Cell Reports
Medicine

Article

Tumor-specific but immunosuppressive CD39$^+$CD8$^+$ T cells exhibit double-faceted roles in clear cell renal cell carcinoma

Graphical abstract

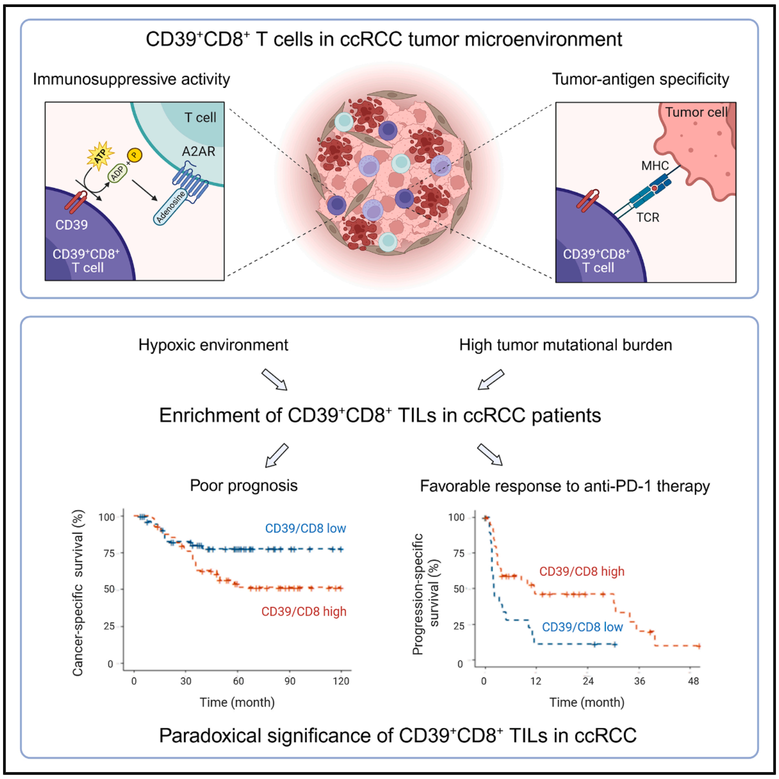

Highlights

- CD39$^+$CD8$^+$ TIL-enriched ccRCC exhibits enhanced hypoxia and high mutation burden
- CD39$^+$CD8$^+$ TILs exert immunosuppression via CD39-dependent adenosine generation
- CD39$^+$CD8$^+$ TIL enrichment predicts poor prognosis in ccRCC
- CD39$^+$CD8$^+$ TIL enrichment predicts favorable anti-PD-1 treatment responses in ccRCC

Authors

Yong Joon Lee, Seung Hyuck Jeon,
Jin Hee Yeo, ..., Minyong Kang,
Seong Il Seo, Eui-Cheol Shin

Correspondence

jjunglammy@yuhs.ac (M.J.),
dr.minyong.kang@gmail.com (M.K.),
siseo@skku.edu (S.I.S.),
ecshin@kaist.ac.kr (E.-C.S.)

In brief

Lee et al. show that CD39$^+$CD8$^+$ tumor-infiltrating T cells are tumor specific but immunosuppressive in ccRCC. CD39$^+$CD8$^+$ T cell-enriched ccRCC tumors exhibit enhanced hypoxic status and high mutational burden. CD39$^+$CD8$^+$ TIL enrichment predicts poor prognosis in ccRCC yet also predicts favorable anti-PD-1 treatment responses, showcasing paradoxical prognostic significance.

Lee et al., 2025, Cell Reports Medicine *6*, 102360
October 21, 2025 © 2025 The Author(s). Published by Elsevier Inc.
https://doi.org/10.1016/j.xcrm.2025.102360

Cell Reports Medicine

CellPress
OPEN ACCESS

Article

Tumor-specific but immunosuppressive CD39$^+$CD8$^+$ T cells exhibit double-faceted roles in clear cell renal cell carcinoma

Yong Joon Lee,[1,2,15] Seung Hyuck Jeon,[2,3,15] Jin Hee Yeo,[1,4,15] Sun-ju Byeon,[5,15] Jae Hyung Jung,[1,2] Heejin Nam,[2] Minwoo Jeon,[1,2] Eui-Soon Kim,[2] Jeon Yeob Jang,[6] Chul-Ho Kim,[6] Kee Yang Chung,[7] Jung Yun Lee,[8] Shin Hwang,[9] Jee Ye Kim,[10] Seung-Il Kim,[10] Jae-Ho Cheong,[10] Chang Gon Kim,[11] Sang Joon Shin,[11] Su-Hyung Park,[2] Minsun Jung,[12,16,*] Minyong Kang,[4,13,14,16,*] Seong Il Seo,[13,16,*] and Eui-Cheol Shin[2,16,17,*]

[1]Department of Surgery, CHA Bundang Medical Center, CHA University School of Medicine, Seongnam, Republic of Korea
[2]Graduate School of Medical Science and Engineering, Korea Advanced Institute of Science and Technology, Daejeon, Republic of Korea
[3]Department of Radiation Oncology, Seoul National University Bundang Hospital, Seongnam, Republic of Korea
[4]Department of Health Sciences and Technology, SAIHST, Sungkyunkwan University, Seoul, Korea
[5]Department of Pathology, Yuseong Sun Hospital, Daejeon, Republic of Korea
[6]Department of Otolaryngology, Ajou University School of Medicine, Suwon, Republic of Korea
[7]Department of Dermatology, Yonsei University College of Medicine, Seoul, Republic of Korea
[8]Department of Obstetrics and Gynecology, Yonsei University College of Medicine, Seoul, Republic of Korea
[9]Department of Surgery, University of Ulsan College of Medicine, Seoul, Republic of Korea
[10]Department of Department of Surgery, Yonsei University College of Medicine, Seoul, Republic of Korea
[11]Division of Medical Oncology, Department of Internal Medicine, Yonsei Cancer Center, Yonsei University College of Medicine, Seoul, Republic of Korea
[12]Department of Pathology, Yonsei University College of Medicine, Seoul, Republic of Korea
[13]Department of Urology, Samsung Medical Center, Sungkyunkwan University School of Medicine, Seoul, Republic of Korea
[14]Translational Genomics Center, Samsung Medical Center, Seoul, Republic of Korea
[15]These authors contributed equally
[16]Senior author
[17]Lead contact
*Correspondence: jjunglammy@yuhs.ac (M.J.), dr.minyong.kang@gmail.com (M.K.), siseo@skku.edu (S.I.S.), ecshin@kaist.ac.kr (E.-C.S.)
https://doi.org/10.1016/j.xcrm.2025.102360

SUMMARY

CD39$^+$CD8$^+$ T cells are known as tumor-antigen-specific cells among CD8$^+$ tumor-infiltrating lymphocytes (TILs). However, CD39$^+$CD8$^+$ T cells also reportedly exhibit immunosuppressive activity in hypoxic tumor models. Here, we investigate CD39$^+$CD8$^+$ TILs in clear cell renal cell carcinoma (ccRCC), a Von Hippel-Lindau (*VHL*) mutation-associated hypoxic tumor. Single-cell analyses confirm that CD39$^+$CD8$^+$ cells are a terminally exhausted subset of tumor-specific CD8$^+$ TILs. CD39$^+$CD8$^+$ T cell development is directly induced by cAMP and T cell receptor (TCR) signaling. Analysis of a renal cell carcinoma (RCC) cohort reveals that the proportion of CD39$^+$CD8$^+$ TILs is associated with a high tumor mutational burden and hypoxic features. *Ex vivo* functional assays reveal that CD39$^+$CD8$^+$ TILs exert immunosuppressive activity via ectonucleotidase activity- and adenosine-dependent mechanisms. CD39$^+$CD8$^+$ TIL enrichment predicts poor prognosis in patients with ccRCC yet also predicts favorable treatment responses to anti-programmed cell death protein 1 (PD-1) therapy. This paradoxical prognostic significance in ccRCC is explained by the dual properties of CD39$^+$CD8$^+$ TILs: tumor antigen specificity and immunosuppressive activity.

INTRODUCTION

Hypoxia is a hallmark of solid tumors and plays roles in tumor progression, tumor aggressiveness, and metastatic changes.[1,2] Across various types of cancers, tumors with hypoxia typically exhibit a poor prognosis, including resistance to chemotherapy, radiotherapy, and immunotherapy. Hypoxia reprograms the tumor microenvironment into an immunosuppressive state through various mechanisms, particularly via the upregulation of hypoxia-sensitive elements, such as hypoxia-inducible factors (HIFs). In response to hypoxia, the overexpression of HIF downstream molecules dampens effective anti-tumor immune responses via a complex interplay of various cellular and molecular mechanisms—including the upregulation of immune checkpoint proteins, induction of immunomodulatory molecules, recruitment of immunosuppressive cells, and regulation of immune cell functions.[3,4]

Among types of renal cell carcinoma (RCC), clear cell renal cell carcinoma (ccRCC) is the most prevalent (70%–80%) and

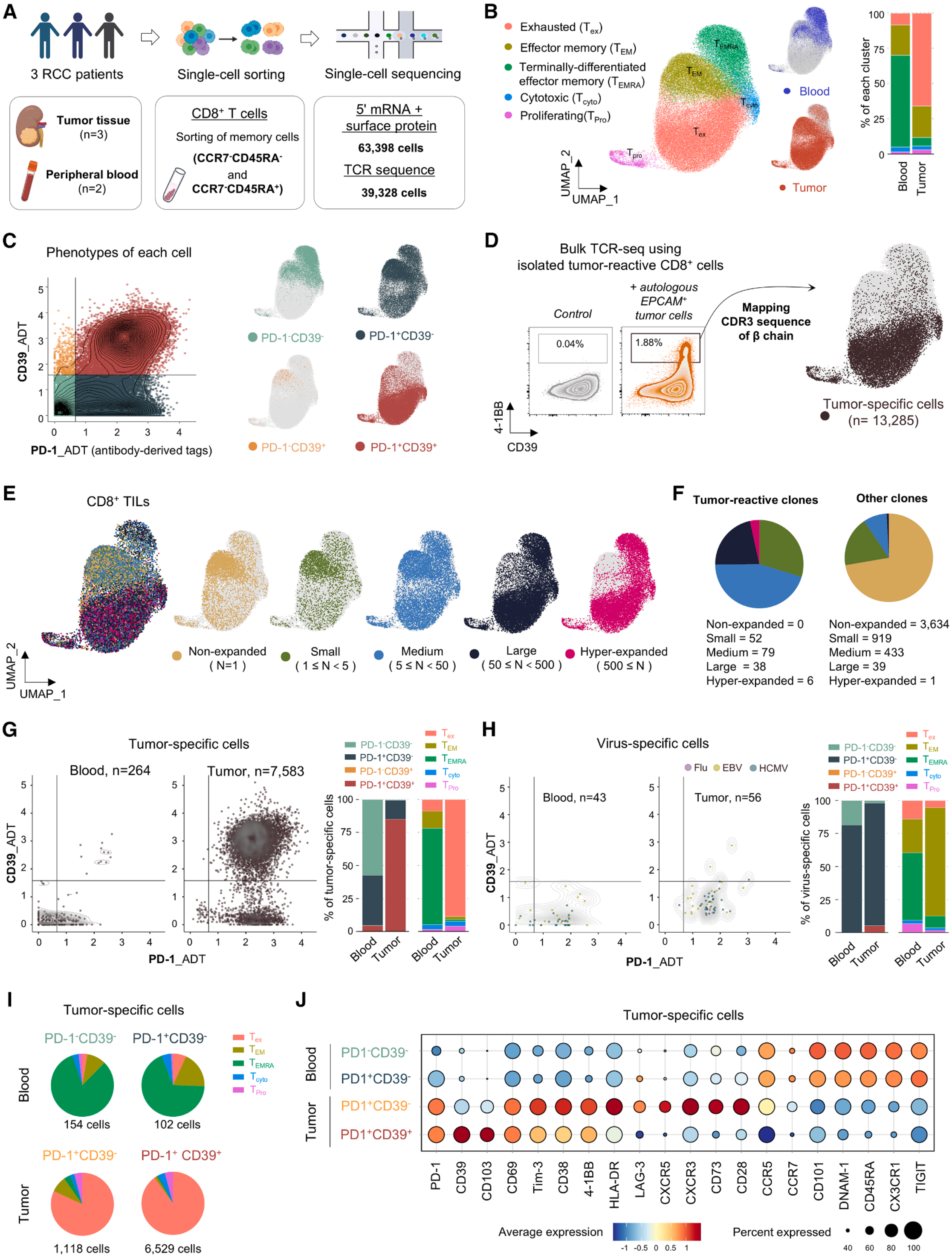

Figure 1. $CD39^+CD8^+$ T cells are terminally exhausted tumor-specific cells within tumors

(A) Scheme of single-cell analysis. Memory $CD8^+$ T cells ($CCR7^-CD45RA^-$ and $CCR7^-CD45RA^+$ subsets) were sorted from samples of three patients with RCC, including tumor tissue (*n* = 3) and peripheral blood (*n* = 2).

(B) Uniform manifold approximation and projection (UMAP) plots of five $CD8^+$ T cell clusters (left), distribution of cells according to the origin (middle), and frequency of each cluster among total cells from each origin (right).

(C) *In silico* gating of $CD8^+$ T cells using antibody-derived tags (ADTs) capturing PD-1 and CD39 (left), and UMAP plots showing the distribution of each subset (right). PD-1 and CD39 expression were classified as positive or negative based on reflection points determined in Figure S1D.

(legend continued on next page)

aggressive subtype and is responsible for the majority of deaths related to kidney cancer.[5,6] Compared to other tumor types, ccRCC tumors are characterized by two distinct features. First, most ccRCC tumors exhibit inactivation of the Von Hippel-Lindau (VHL) protein, through biallelic loss of the *VHL* tumor suppressor gene, which induces the accumulation of HIFs and downstream proteins.[7,8] Thus, ccRCC exhibits typical features of hypoxic tumors, including enhancement of the adenosine signaling pathway and angiogenesis pathway.[9–11] Second, unlike in other human cancers, in ccRCC, high numbers of tumor-infiltrating CD8$^+$ T cells are associated with a poorer prognosis,[12–14] the mechanism of which remains unknown. Considering that CD8$^+$ T cells typically exert cytotoxicity against tumor cells, this negative impact of CD8$^+$ T cells in ccRCC seems paradoxical, even if these cells are functionally impaired or exhausted.

Among tumor-infiltrating CD8$^+$ T cells, CD39$^+$CD8$^+$ T cells are considered tumor-antigen-specific cells. Several studies have demonstrated that CD39 expression distinguishes tumor-antigen-specific CD8$^+$ T cells from the tumor-unrelated bystander CD8$^+$ T cells that are abundant among tumor-infiltrating lymphocytes (TILs).[15–17] On the other hand, a recent study has highlighted the immunosuppressive activity of CD39$^+$CD8$^+$ T cells, which is mediated by CD39-dependent adenosine generation.[18] *In vitro* hypoxia induces CD39 expression on terminally exhausted CD8$^+$ T cells, and CD39 deletion in CD8$^+$ T cells results in restricted tumor growth and improved efficacy of immunotherapy in mouse tumor models.[18] However, prognostic analyses of human cancer do not support an immunosuppressive role of CD39$^+$CD8$^+$ T cells. In fact, several studies in various types of human cancers show that high numbers of tumor-infiltrating CD39$^+$CD8$^+$ T cells are associated with a favorable prognosis and with a good response to treatment with immune checkpoint blockades (ICBs).[17,19–23]

In the present study, we examined tumor-infiltrating CD39$^+$CD8$^+$ T cells with regard to their molecular phenotypes, developmental mechanisms, functions, and prognostic significance, using ccRCC as a typical hypoxic tumor. We confirmed that tumor-infiltrating CD39$^+$CD8$^+$ T cells exhibited both tumor antigen specificity and immunosuppressive activity. Additionally, we found that CD39 was upregulated in tumor-infiltrating CD8$^+$ T cells in the context of high tumor mutations and hypoxic environment. Notably, we verified that tumor-infiltrating CD39$^+$CD8$^+$ T cells have paradoxical effects on tumor recurrence and treatment response to ICBs in ccRCC, stemming from their two distinct features: tumor antigen specificity and immunosuppressive activity. Therefore, enrichment of tumor-infiltrating CD39$^+$CD8$^+$ T cells predicts a high potential for tumor recurrence, as well as a favorable response to anti-PD-1 treatment.

RESULTS

CD39$^+$CD8$^+$ T cells are terminally exhausted tumor-specific cells within tumors

Using specimens from three patients with ccRCC, we performed single-cell RNA sequencing (scRNA-seq) based on the cellular indexing of transcriptomes and epitopes sequencing technique, combined with single-cell T cell receptor (TCR) sequencing (Figure 1A). We enriched memory CD8$^+$ T cells (CCR7$^-$CD45RA$^-$ and CCR7$^-$CD45RA$^+$ CD8$^+$ T cells) from single-cell suspensions of tumor tissues ($n = 3$) and peripheral blood mononuclear cells (PBMCs; $n = 2$). We captured a total of 63,398 cells, each with matched transcriptome and proteome information after quality control. TCR sequences were retrieved from 39,328 cells. Based on mRNA expression, we identified five clusters: exhausted (T$_{ex}$), effector memory, terminally differentiated effector memory (T$_{EMRA}$), cytotoxic, and proliferating CD8$^+$ T cells (Figures 1B and S1A). Antibody-derived tag (ADT) analysis revealed that T$_{ex}$ cells expressed immune checkpoint receptors (e.g., PD-1 and T-cell immunoglobulin and mucin-domain containing-3 [TIM-3]) and T cell activation markers (e.g., 4-1BB, human leukocyte antigen [HLA]-DR, and CD38) (Figure S1B). The proportion of T$_{ex}$ cells was higher in tumors compared to blood (Figures 1B and S1C). Each cell was categorized into four subpopulations, according to ADT-labeled PD-1 and CD39 expressions: PD-1$^-$CD39$^-$, PD-1$^+$CD39$^-$, PD-1$^-$CD39$^+$, and PD-1$^+$CD39$^+$ cells (Figures 1C and S1D). PD-1$^+$CD39$^+$ cells were predominantly found in tumors, and most of those were T$_{ex}$ cells (Figures S1E and S1F).

To identify tumor-specific CD8$^+$ T cells, we sorted CD39$^-$CD8$^+$ and CD39$^+$CD8$^+$ TILs and co-cultured these cells with autologous epithelial cell adhesion molecule (EPCAM)$^+$ cells (Figure S2A). We confirmed increased frequencies of interferon (IFN)-γ^+ and 4-1BB$^+$ cells among co-cultured CD39$^+$CD8$^+$ TILs (Figures S2B and S2C) and then sorted tumor-reactive 4-1BB$^+$ cells from co-cultured CD39$^+$CD8$^+$ TILs and performed bulk TCR sequencing (TCR-seq) analysis (Figure 1D). Clonotypes were considered tumor specific if a β-chain CDR3 from scRNA-seq was identified among the bulk TCR-seq results from tumor-reactive 4-1BB$^+$CD39$^+$ cells. Among total 6,264 clones, 182 clones shared identical β-chain CDR3 sequences

---

(D) Schematic illustrating bulk TCR sequencing of tumor-reactive 4-1BB$^+$CD39$^+$CD8$^+$ TILs after co-culturing with autologous tumor cells (EPCAM$^+$ cells) and identification of tumor-specific cells by mapping tumor-reactive clonotypes onto the single-cell sequencing data.

(E) CD8$^+$ TILs are visualized using UMAP and color-coded based on clonal expansion. Each dot represents a single CD8$^+$ T cell.

(F) Pie charts show the distribution of clonal expansion levels in TILs for tumor-reactive clones (left, 175 clones) and all other non-reactive clones (right, 5,026 clones).

(G) PD-1 and CD39 protein expression in tumor-specific CD8$^+$ T cells (left). Bar plots show their distribution according to PD-1 and CD39 protein expression (middle) and across transcriptome-based clusters (right) in both blood and tumor.

(H) PD-1 and CD39 protein expression in virus-specific CD8$^+$ T cells (left). Bar plots show their distribution according to PD-1 and CD39 protein expression (middle) and across transcriptome-based clusters (right) in both blood and tumor.

(I) Pie charts show the distribution of five transcriptional clusters within each subpopulation of tumor-specific CD8$^+$ T cells classified by PD-1 and CD39 expression in blood and tumor.

(J) Pattern of ADT expression in each subpopulation of tumor-specific CD8$^+$ T cell classified by PD-1 and CD39 expression.

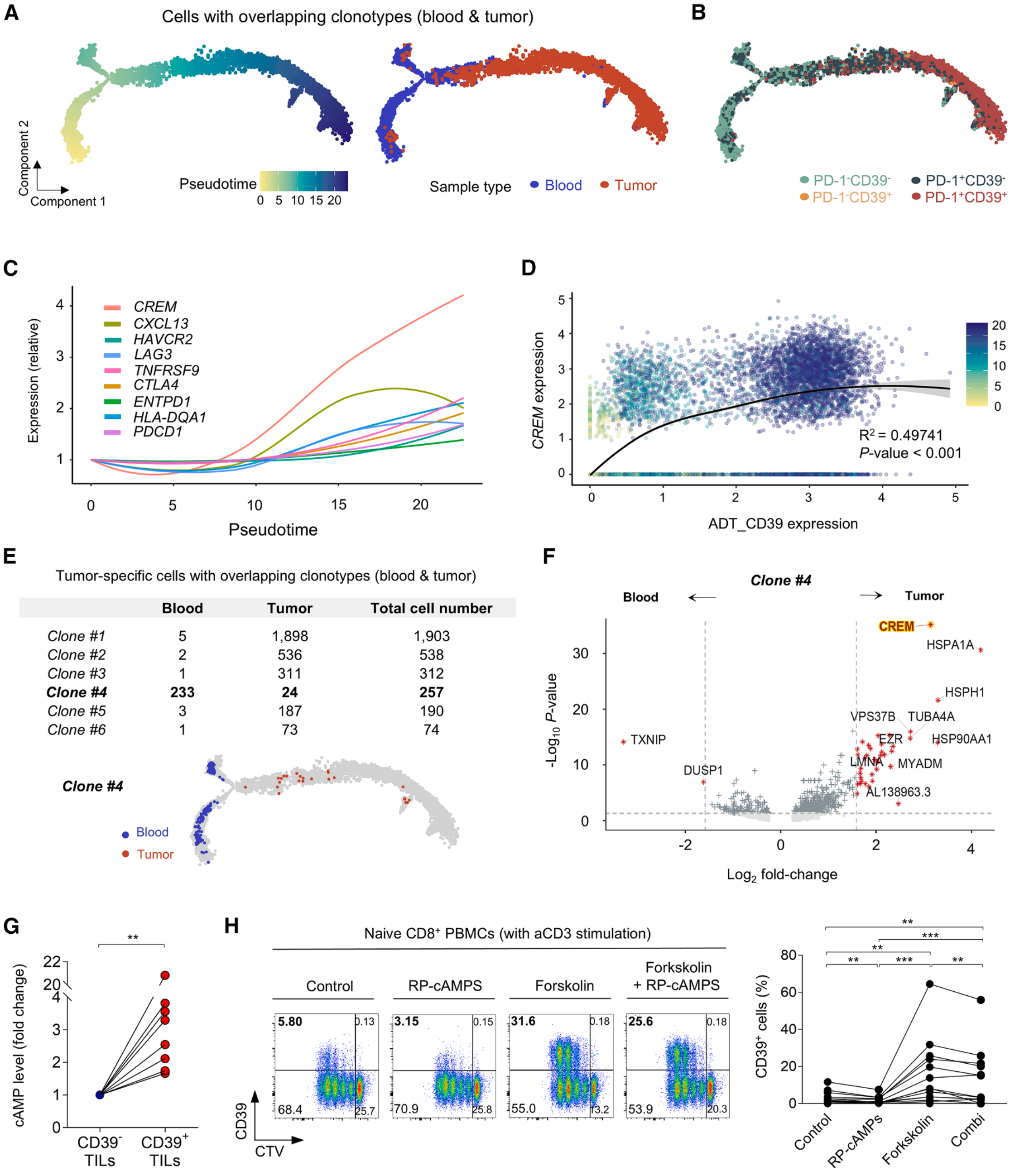

Tumor-specific cells with overlapping clonotypes (blood & tumor)

	Blood	Tumor	Total cell number
Clone #1	5	1,898	1,903
Clone #2	2	536	538
Clone #3	1	311	312
Clone #4	**233**	**24**	**257**
Clone #5	3	187	190
Clone #6	1	73	74

Figure 2. Tumor-infiltrating CD39$^+$CD8$^+$ T cells exhibit enhanced cAMP and TCR signaling

(A and B) The ordering of CD8$^+$ T cells with clonotypes that overlap between peripheral blood and tumor along pseudotime. (A) Annotated with the pseudotime ordering (left) and sample origin (right). (B) Annotated with CD8$^+$ T cell subpopulations classified by PD-1 and CD39 expression.

(C) Relative expression of selected genes related to T cell differentiation, according to the pseudotime.

(D) Relative *CREM* expression according to the CD39 ADT expression. Trend line and error are for linear regression with 95% CI. Pearson's R^2 and two-sided p value are listed.

(E) Table showing the number of cells for six tumor-specific T cell clones shared between blood and tumor (top). Clone #4 was the most abundant in blood ($n = 233$) and was also detected at relatively high frequency in tumor ($n = 24$). Distribution of clone #4 cells along the pseudotime trajectory (bottom).

(F) Volcano plot showing differential gene expression between tumor-specific CD8$^+$ T cells of clone #4 from blood and tumor.

(G) Relative concentration of intracellular cAMP within CD39$^-$ and CD39$^+$CD8$^+$ TILs ($n = 8$). Fold change values are shown relative to CD39$^-$CD8$^+$ TILs within each sample. **$p < 0.01$ by Wilcoxon matched-pairs signed-rank test.

(legend continued on next page)

with bulk TCR-seq results from tumor-reactive 4-1BB$^+$CD39$^+$ cells. We further validated the tumor specificity of identified CD8$^+$ T cell clonotypes by analyzing their clonal expansion. Among CD8$^+$ TILs, T cell clones were classified as non-expanded ($n = 1$), small ($1 \leq n < 5$), medium ($5 \leq n < 50$), large ($50 \leq n < 500$), or hyper-expanded ($n \geq 500$) (Figure 1E). Notably, the 175 tumor-reactive clones were expanded clones, with none falling into the non-expanded category, and exhibited significantly greater clonal expansion compared to the other non-reactive clones (Figure 1F), supporting their tumor specificity.

Tumor-specific CD8$^+$ T cells were mainly PD-1$^+$CD39$^-$ or PD-1$^+$CD39$^+$ in tumors but were mainly PD-1$^-$CD39$^-$ or PD-1$^+$CD39$^-$ in blood (Figure 1G). Additionally, the majority of tumor-specific CD8$^+$ T cells were T_{EMRA} cells in blood but were T_{ex} cells in tumor. Tumor-unrelated virus-specific cells were identified by matching clonotypes with a public database (Figure S2D) and were largely PD-1$^+$CD39$^-$ cells in both blood and tumor and lacked T_{ex} cells (Figure 1H). Tumor-specific PD-1$^+$CD39$^+$CD8$^+$ T cells in tumor exhibited terminally differentiated features, including high expressions of *CXCL13*, *LAG3*, and TIM-3 and low expressions of CXCR5 and CD28 (Figures 1I, 1J and S3A). We used a class I major histocompatibility complex multimer to detect CD8$^+$ TILs specific to carbonic anhydrase IX (CAIX), a tumor-associated antigen. Compared to CAIX-specific CD39$^-$CD8$^+$ TILs, CAIX-specific CD39$^+$CD8$^+$ TILs exhibited lower frequencies of TCF-1$^+$ cells (Figures S3B and S3C). Subsequent *in vitro* functional analysis indicated that CD39$^+$PD-1^{bright}CD8$^+$ TILs exhibited reduced capacities for cytokine production and proliferation upon TCR stimulation, compared to CD39$^-$PD-1^{bright}CD8$^+$ TILs (Figure S3D). Analysis of a publicly available scRNA-seq dataset[24] further supported that CD39$^+$PD-1$^+$ CD8$^+$ T cells exhibit transcriptional profiles consistent with tumor-specific, exhausted T cells (Figure S3E). Taken together, our results indicated that CD39$^+$CD8$^+$ TILs constitute tumor-specific CD8$^+$ T cells displaying characteristics of terminal exhaustion.

Tumor-infiltrating CD39$^+$CD8$^+$ T cells exhibit enhanced cAMP and TCR signaling

To explore lineage relationships between CD8$^+$ T cell subpopulations, we conducted pseudotime analysis on cells with overlapping clonotypes between blood and tumor, using the same scRNA-seq dataset as in Figure 1. The inferred trajectory revealed sequential changes from blood CD8$^+$ T cells to tumor-infiltrating CD8$^+$ T cells (Figure 2A) and from the PD-1$^-$CD39$^-$ state to the PD-1$^+$CD39$^-$ state, ultimately culminating in the PD-1$^+$CD39$^+$ state (Figure 2B). To track the molecular changes occurring during differentiation, we examined genes exhibiting a strong correlation with pseudotime (Table S1). The *CREM* (cAMP-responsive element modulator) gene was among the genes most highly correlated with pseudotime (Figure 2C). Interestingly, *CREM* gene expression exhibited a more pronounced increase in the pseudotime trajectory, compared to genes with well-established linkage to T cell differentiation, including *PDCD1*, *CXCL13*, *LAVCR2*, *LAG3*, *TNFRSF9*, *CTLA-4*, *ENTPD1*, and *HLA-DQA1*. Moreover, *CREM* expression was significantly associated with CD39 expression (Figure 2D), implying its relevance to the process of differentiation into PD-1$^+$CD39$^+$ cells in the tumor environment.

To precisely calibrate the molecular alterations within tumor-specific clones, we identified six tumor-specific CD8$^+$ T cell clones exhibiting overlapping clonotypes between blood and tumor (Figure 2E). Among these, we focused on a single clone (*clone #4*), which displayed relatively high numbers of cells in both blood (233 cells) and tumor (24 cells), enabling differential expression gene analysis. Of particular interest, tumor-specific *clone #4* T cells exhibited significantly higher *CREM* expression in tumor compared to their counterparts in blood, underscoring the developmental significance of *CREM* in the tumor environment (Figure 2F).

Since *CREM* expression is induced by cAMP signaling activation and serves as a mediator for transcribing cAMP-responsive genes, we further examined whether CD39 expression on tumor-infiltrating CD8$^+$ T cells was influenced by cAMP signaling that was known to be associated with hypoxia.[25–27] First, we observed that CD39$^+$CD8$^+$ TILs exhibited higher intracellular cAMP levels than CD39$^-$CD8$^+$ TILs (Figure 2G). Next, we sorted CCR7$^+$CD45RA$^+$ naive CD8$^+$ T cells from PBMCs, stimulated them using anti-CD3 antibodies, and observed that only a subset of CD8$^+$ T cells expressed CD39 (Figure 2H). Treatment with a cAMP-elevating agent (forskolin) markedly upregulated CD39 expression, while the addition of a cAMP-reducing agent (RP-cAMPS) abrogated the CD39-upregulating effect of forskolin. Notably, the effect of forskolin on CD39 upregulation was exclusively evident in CD8$^+$ T cells that underwent more than three cycles of division following anti-CD3 stimulation (Figure S3F). Furthermore, treatment with forskolin alone, without anti-CD3 stimulation, did not increase the CD39 expression on CD8$^+$ T cells (Figure S3G). These results suggested that cAMP signaling selectively functioned in differentiating CD8$^+$ T cells in response to antigen stimulation. Taken together, our findings indicated that tumor-specific CD39$^+$CD8$^+$ T cells exhibited enhanced cAMP signaling, as well as TCR signaling, in ccRCC tumors.

CD39$^+$CD8$^+$ T cell-enriched ccRCC tumors are characterized by higher tumor mutational burden and enhanced hypoxic status

Next, we performed flow cytometry analysis to compare the proportions of CD39$^+$CD8$^+$ T cells among CD8$^+$ TILs obtained from various cancer types (Figure 3A; Table S2) and found that ccRCC exhibited one of the highest proportions of CD39$^+$CD8$^+$ T cells. Notably, the proportion of CD39$^+$CD8$^+$ T cells was significantly higher in ccRCC compared to other RCC subtypes, including

---

(H) CD39 expression in naive CD8$^+$ T cells from PBMCs following anti-CD3 stimulation under indicated conditions: control, RP-cAMPS (cAMP-reducing agent), forskolin (cAMP-elevating agent), and forskolin + RP-cAMPS. Representative flow cytometry plots are shown on the left. The graph on the right shows the proportion of CD39$^+$ cells under each condition, with data points from the same donor connected by lines. Pairwise Wilcoxon signed-rank tests with Benjamini-Hochberg correction for multiple comparisons.

$^{**}p < 0.01$, $^{**}p < 0.01$, and $^{***}p < 0.001$.

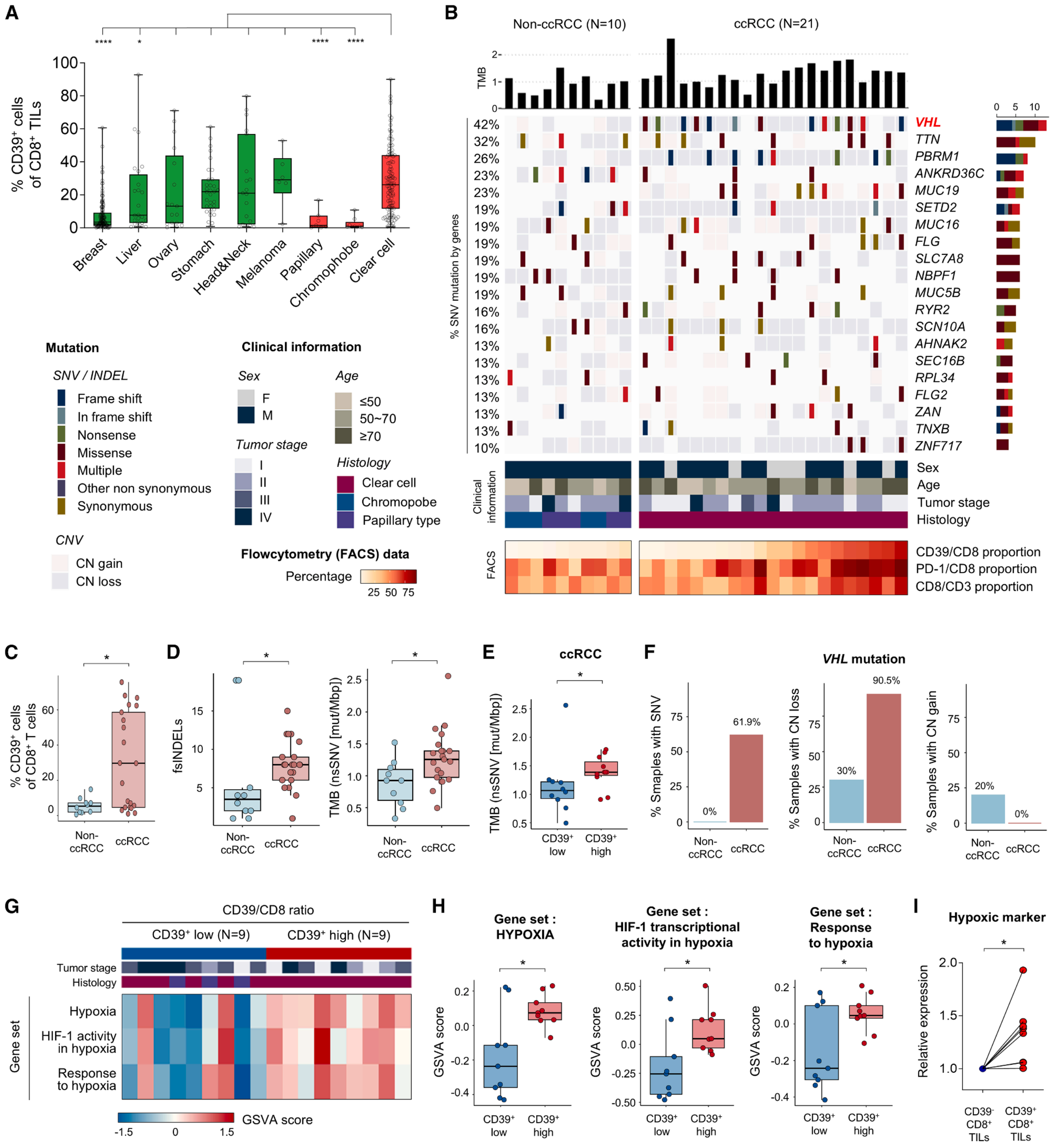

Figure 3. $CD39^+CD8^+$ T cell-enriched ccRCC tumors are characterized by higher TMB and enhanced hypoxic status

(A) Proportions of $CD39^+$ cells among $CD8^+$ TILs across various cancer types: breast ($n = 131$), liver ($n = 24$), ovary ($n = 17$), stomach ($n = 32$), head and neck ($n = 19$), melanoma ($n = 6$), papillary RCC ($n = 7$), chromophobe RCC ($n = 9$), and ccRCC ($n = 112$).

(B–F) WES data of 31 patients with RCC (ccRCC, $n = 21$; non-ccRCC, $n = 10$). (B) Summary of somatic mutation and copy-number variation of select genes, clinical information, and flow cytometry data. Bar plots at the top represent the TMB for each patient. The central heatmap displays the top 20 genes with the highest frequency of single-nucleotide variant (SNV) mutations across all samples, ordered by prevalence. Mutation types are color-coded based on SNV/INDEL categories and copy-number variations as indicated in the left. Clinical characteristics are shown directly beneath the mutation matrix. At the bottom, a heatmap represents flow cytometry-based immune profiling data. (C) Proportion of $CD39^+$ cells among $CD8^+$ TILs according to the histology of RCC. (D) Number of frameshift insertions and deletions (fsINDELs; left), and non-synonymous single-nucleotide variants (nsSNV) per megabase pair (right) according to the histology

(legend continued on next page)

papillary or chromophobe types. This result was supported by The Cancer Genome Atlas analysis for the expression of *ENTPD1*, a gene for CD39. *ENTPD1* was among the highest in ccRCC (Figure S4A) and was low in other RCC subtypes, including papillary or chromophobe types.

To further investigate ccRCC-specific molecular characteristics, we performed whole-exome sequencing (WES) using 31 RCC tumor tissues and their paired normal tissues (Figure S4B), including 21 ccRCC and 10 non-ccRCC subtypes (i.e., chromophobe and papillary). Our analysis included the calculation of tumor mutational burden (TMB), measurement of frameshift insertions or deletions (fsINDELs), identification of somatic mutations, and assessment of copy-number variations. We also integrated WES data with clinicopathologic characteristics and CD8$^+$ T cell profiling achieved by flow cytometry analysis (Figures 3B; Table S3).

The ccRCC and non-ccRCC subtypes did not significantly differ in the proportion of CD8$^+$ T cells among CD3$^+$ T cells or the proportion of PD-1$^+$ cells among CD8$^+$ T cells, while the proportion of CD39$^+$ cells among CD8$^+$ T cells was markedly elevated in ccRCC compared to non-ccRCC (Figures 3C and S4C). Compared to non-ccRCC subtypes, ccRCC exhibited significantly higher fsINDELs and TMB (Figure 3D). Among ccRCC, tumors with a higher proportion of CD39$^+$CD8$^+$ T cells exhibited higher TMB, compared to tumors with a lower proportion of CD39$^+$CD8$^+$ T cells (Figures 3E and S4D). Other parameters related to tumor antigenicity, such as HLA homozygosity or heterozygosity, were comparable between ccRCC and non-ccRCC tumors (Figure S4E). Notably, mutations of the *VHL* gene were exclusively observed in ccRCC tumors and were absent from non-ccRCC tumors (Figure 3F). Additionally, copy-number loss of the *VHL* gene was more frequently present in ccRCC, compared to non-ccRCC tumors.

To investigate the hypoxic state of tumors, we performed bulk mRNA sequencing (RNA-seq) using 18 RCC tumor tissues, including 15 ccRCC and 3 non-ccRCC subtypes (Figure S4B; Table S4). These samples were categorized into two groups based on the proportion of CD39$^+$ cells among CD8$^+$ T cells, and we compared the expression levels of various hypoxia-associated gene sets between the CD39-high and -low groups (Figure 3G). The CD39-high group exclusively included ccRCC and exhibited significantly higher expressions of hypoxia-related gene sets, compared to the CD39-low group (Figure 3H). Expression of hypoxia-related gene sets did not differ according to tumor stages (Figure S4F). Flow cytometry analysis was performed using a dye to assess oxygen levels, revealing that CD39$^+$CD8$^+$ TILs exhibited a more hypoxic status compared to CD39$^-$CD8$^+$ TILs (Figure 3I). Collectively, these observations established an association between a hypoxic state and the enrichment of CD39$^+$CD8$^+$ T cells within ccRCC tumors.

CD39$^+$CD8$^+$ TILs exhibit CD39-dependent immunosuppressive activity

CD39 exerts ectonucleotidase activity, hydrolyzing ATP or ADP to AMP, which is ultimately hydrolyzed to adenosine by CD73. Since adenosine suppresses various types of immune cells, CD39 is considered an immunosuppressive molecule. The immunosuppressive activity of CD39 has been well described in studies of CD39$^+$ regulatory T cells.[28,29] In this background, we wondered whether CD39$^+$CD8$^+$ T cells might contribute to the immunosuppressive tumor environment in ccRCC. We first examined which T cell population was the main one contributing to CD39 expression among TILs. Among CD39$^+$CD45$^+$ TILs from ccRCC, we found that the frequency of CD8$^+$ T cells was significantly higher than that of Foxp3$^+$ or Foxp3$^-$ CD4$^+$ TILs (Figure 4A). Further analysis of various cancer types demonstrated that ccRCC exhibited one of the highest proportions of CD8$^+$ T cells among CD39$^+$CD45$^+$ TILs (Figure 4B; Table S2). Also, the proportion of CD8$^+$ T cells among CD39$^+$CD45$^+$ TILs was significantly higher in ccRCC compared to other RCC subtypes, including papillary or chromophobe types.

Next, we directly examined the immunosuppressive activity of CD39$^+$CD8$^+$ TILs from ccRCC. For the ectonucleotidase activity assay, we cultured sorted CD39$^+$CD8$^+$ TILs, CD39$^-$CD8$^+$ TILs, and CD8$^+$ PBMCs with exogenous ATP and serially measured ATP levels in the culture medium (Figure 4C). ATP levels were dramatically reduced in the culture of CD39$^+$CD8$^+$ TILs, which was not observed in CD8$^+$ PBMCs and CD39$^-$CD8$^+$ TILs. This decrease was negated by co-incubation with a chemical inhibitor of CD39, confirming the ectonucleotidase activity of CD39 expressed on CD8$^+$ TILs. We subsequently assessed the anti-CD3-stimulated cytokine production from CD8$^+$ PBMCs, upon co-culture with autologous CD39$^+$CD8$^+$ TILs. In the presence of exogenous ATP, CD8$^+$ PBMCs co-cultured with CD39$^+$CD8$^+$ TILs exhibited significantly reduced IFN-γ and tumor necrosis factor (TNF) production. However, the addition of a CD39 inhibitor restored the decreased cytokine production of CD8$^+$ PBMCs, indicating CD39-mediated immunosuppression by CD39$^+$CD8$^+$ TILs (Figure 4D). Moreover, we observed consistent results when the same co-culture assay was conducted using CD39$^-$PD-1$^{\text{bright}}$CD8$^+$ TILs as responder cells and CD39$^+$PD-1$^{\text{bright}}$CD8$^+$ TILs as suppressor cells (Figure 4E).

The immunosuppressive activity of CD39$^+$CD8$^+$ TILs was further assessed in a co-culture system in which TILs were reconstituted without a CD39 source from non-CD8$^+$ TILs. To

of RCC. (E) Number of nsSNV per megabase pair in ccRCC according to CD39 expression level on CD8$^+$ TILs: CD39$^+$ low (n = 10) and CD39$^+$ high (n = 11). (F) Proportion of samples with SNV (left), copy-number loss (middle), and copy-number gain (right) in *VHL* gene according to the histology of RCC.

(G and H) WTS data of 18 patients with RCC (ccRCC, n = 15; non-ccRCC, n = 3). (G) Heatmap showing gene set variation analysis (GSVA) scores for hypoxia-related gene sets in each patient, stratified by CD39$^+$CD8$^+$ T cell proportion (CD39$^+$ low, n = 9 vs. CD39$^+$ high, n = 9). Tumor stage and histology are annotated above the heatmap, as defined in (B). (H) Boxplots comparing GSVA scores for hypoxia-related gene sets between the two groups.

(I) Expression of a hypoxic marker was assessed using Hypoxia Green Reagent, a dye that measures oxygen levels, by flow cytometry in CD39$^-$CD8$^+$ TILs and CD39$^+$CD8$^+$ TILs (n = 8). The relative expression was calculated based on the mean fluorescence intensity.

Data are represented as median with interquartile range; whiskers indicate the minimum and maximum values (A, C, D, E, and H).

$^*p < 0.05$, $^{**}p < 0.01$, $^{***}p < 0.001$, and $^{****}p < 0.0001$ by two-sided Mann-Whitney U test (A, C, D, E, and H) and Wilcoxon matched-pairs signed rank test (I).

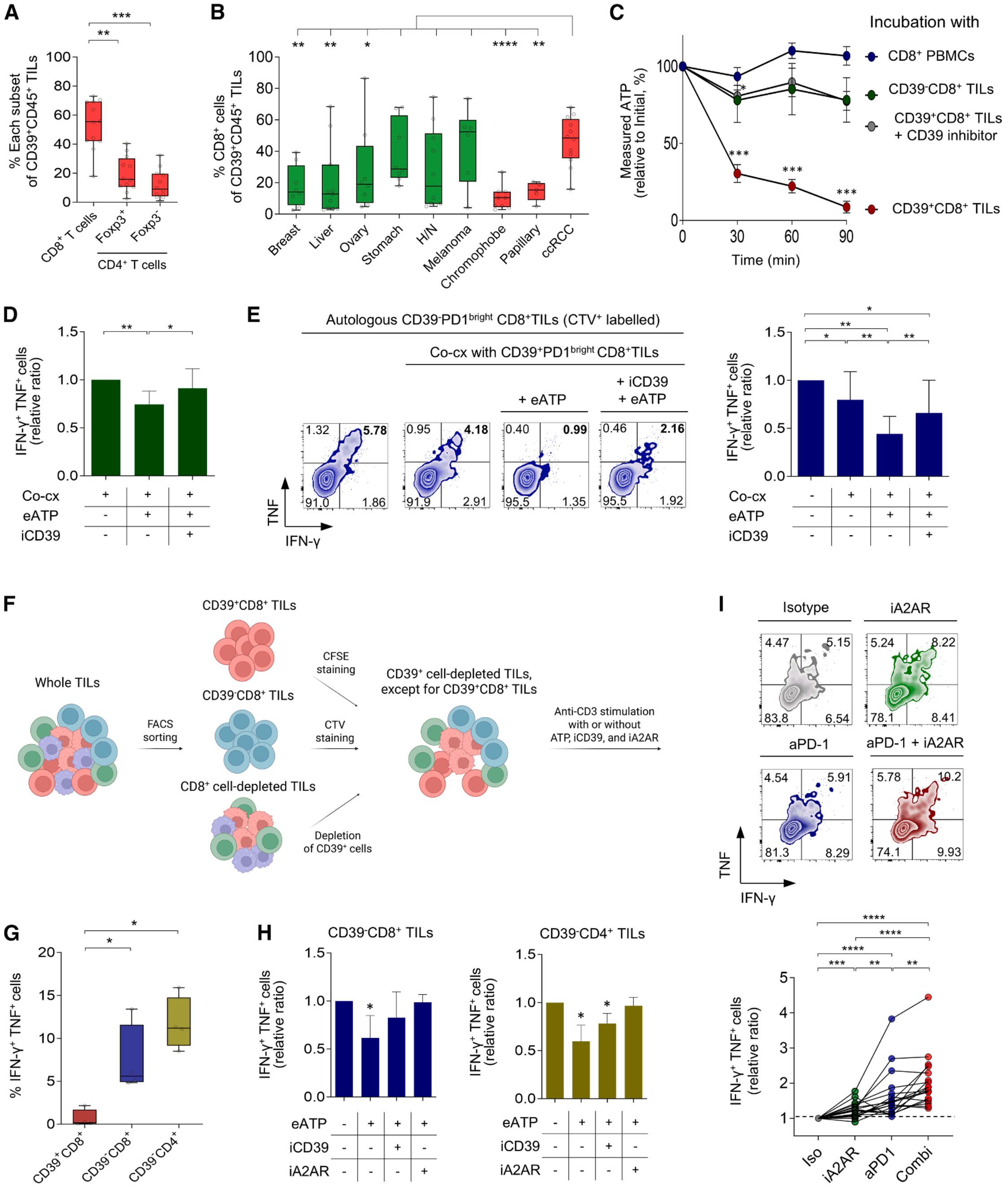

Figure 4. CD39$^+$CD8$^+$ TILs exhibit CD39-dependent immunosuppressive activity

(A) Proportions of each T cell subset among tumor-infiltrating CD39$^+$CD45$^+$ immune cells in ccRCC (*n* = 12).

(B) Proportions of CD8$^+$ TILs among tumor-infiltrating CD39$^+$CD45$^+$ immune cells across various cancer types: breast (*n* = 8), hepatocellular carcinoma (*n* = 11), ovary (*n* = 8), stomach (*n* = 8), head and neck (*n* = 10), melanoma (*n* = 6), chromophobe RCC (*n* = 9), papillary RCC (*n* = 5), and ccRCC (*n* = 12).

(C) ATP concentrations were serially measured in culture medium after the indicated cells were cultured in the presence of exogenous ATP, with or without CD39 inhibitor (*n* = 6).

(D) Relative proportions of IFN-γ$^+$TNF$^+$ cells among CD8$^+$ PBMCs upon anti-CD3 stimulation (*n* = 8). CD8$^+$ PBMCs were co-cultured with CD39$^+$PD-1^{bright}CD8$^+$ TILs in the presence or absence of extracellular ATP (eATP) or a CD39 inhibitor (iCD39).

(E) Relative proportions of IFN-γ$^+$TNF$^+$ cells among CD39$^-$PD-1^{bright}CD8$^+$ TILs upon anti-CD3 stimulation (*n* = 12). CD39$^-$PD-1^{bright}CD8$^+$ TILs were co-cultured with CD39$^+$PD-1^{bright}CD8$^+$ TILs in the presence or absence of eATP or iCD39.

(F–H) Cytokine production assay in a co-culture system, where TILs were reconstituted without a CD39 source from non-CD8$^+$ TILs (*n* = 4). (F) Experimental schematic for reconstitution of TILs in which CD39 is expressed only among CD8$^+$ TILs. (G) Proportions of IFN-γ$^+$TNF$^+$ cells upon anti-CD3 stimulation in each

(legend continued on next page)

avoid the effects of CD39$^+$ cells among non-CD8$^+$ TILs, we depleted CD39$^+$ cells (except CD39$^+$CD8$^+$ T cells) from single-cell suspensions of tumors and then stimulated these cells using anti-CD3, with or without a CD39 inhibitor or an adenosine 2A receptor (A2AR) inhibitor (Figure 4F). IFN-γ and TNF were produced from CD39$^-$CD8$^+$ TILs and CD39$^-$CD4$^+$ TILs but not from CD39$^+$CD8$^+$ TILs, in accordance with the terminally exhausted features of CD39$^+$CD8$^+$ TILs (Figure 4G). Exogenous ATP decreased cytokine production from CD39$^-$CD8$^+$ TILs and CD39$^-$CD4$^+$ TILs, and this decrease was reversed by both CD39 and A2AR inhibitors (Figure 4H). These results confirmed that CD39$^+$CD8$^+$ TILs suppress neighboring T cells in an ATP-enriched environment, through a mechanism that is dependent on adenosine and A2AR.

Finally, to investigate whether an A2AR inhibitor could restore effector functions of CD8$^+$ TILs, we performed an *ex vivo* T cell assay using tumor single-cell suspensions from ccRCC, with or without an A2AR inhibitor and anti-PD-1 treatment (Figure 4I). The cytokine production of CD8$^+$ TILs was significantly increased by an A2AR inhibitor or anti-PD-1 blockade, and this effect was further enhanced by their combinational treatment. These findings demonstrated that both adenosine signaling and the PD-1/programmed death-ligand 1 (PD-L1) axis contribute to the immunosuppressive tumor environment in ccRCC.

Enrichment of CD39$^+$CD8$^+$ TILs predicts poor prognosis of patients with ccRCC

We investigated whether enrichment of CD39$^+$CD8$^+$ TILs was associated with prognosis in patients with ccRCC. Multiplex immunohistochemistry (IHC) for CD8 and CD39 was performed using formalin-fixed and paraffin-embedded (FFPE) tissues obtained from surgical tumor specimens of patients with ccRCC with disease of pathologic T (pT) stage III or higher (n = 110) (Figure 5A; Table S5), and the proportion of CD39$^+$ cells among CD8$^+$ TILs was quantified (Figure 5B). Importantly, the proportion of CD39$^+$ cells among CD8$^+$ TILs was generally unaffected by clinicopathologic characteristics that can influence patient prognosis—including pT stage, pathologic node metastasis stage, and distant metastasis at diagnosis (Figures S5A–S5C).

Patients were categorized into two groups based on the median proportion of CD39$^+$ cells among CD8$^+$ TILs. Overall, patients with high proportions of CD39$^+$ cells among CD8$^+$ TILs exhibited significantly worse cancer-specific survival, compared to patients with low proportions of CD39$^+$ cells among CD8$^+$ TILs (Figure 5C). Those who experienced tumor recurrence after surgery exhibited significantly higher proportions of CD39$^+$ cells among CD8$^+$ TILs, compared to those without tumor recurrence (Figure 5D).

We next investigated whether the prognostic utility of the proportion of CD39$^+$ cells among CD8$^+$ T cells for predicting cancer-specific survival was independent of other clinicopathological factors associated with cancer patient prognosis. We used the receiver operating characteristic (ROC) curve to determine the optimal cutoff value for the proportion of CD39$^+$ cells among CD8$^+$ TILs (Figure 5E). Multivariable Cox regression analysis revealed that, while the total number of CD8$^+$ TILs was not a significant prognostic factor, the CD39$^+$ cell proportion among CD8$^+$ TILs was an independent prognostic factor for cancer-specific survival among patients with ccRCC (p value = 0.03; hazard ratio [HR], 2.27; 95% confidence interval [CI], 1.08–4.80) (Figure 5F).

Enrichment of CD39$^+$CD8$^+$ TILs predicts favorable treatment response to anti-PD-1 therapy

Next, we assessed the prognostic value of CD39$^+$CD8$^+$ TIL enrichment in the context of anti-PD-1 treatment. We identified patients with metastatic ccRCC who received first-line (n = 15) or second-line (n = 44) anti-PD-1 treatment after surgery and collected FFPE tissues from surgical tumor specimens of those patients (Figure 6A; Table S6). We performed multiplex IHC for CD8 and CD39 and quantified the proportion of CD39$^+$ T cells among CD8$^+$ TILs. The objective response was determined as the best response post treatment, according to radiologic assessment, adhering to the Response Evaluation Criteria in Solid Tumors, which includes complete response (CR), partial response (PR), stable disease (SD), and progressive disease (PD). Compared to patients with PD, patients with CR, PR, and SD exhibited significantly higher counts of CD39$^+$CD8$^+$ TILs (Figure 6B).

According to the cutoff value for the proportion of CD39$^+$ cells among CD8$^+$ TILs (determined in Figure 5E), patients in the anti-PD-1 cohort were categorized into high (n = 40) and low (n = 19) groups. Patients with high proportions of CD39$^+$ cells among CD8$^+$ TILs exhibited significantly better progression-free survival after anti-PD-1 treatment, compared to those with low proportions of CD39$^+$ cells among CD8$^+$ TILs (Figure 6C). Multivariable Cox regression analysis revealed that the proportion of CD39$^+$ cells among CD8$^+$ TILs was an independent prognostic factor for favorable progression-free survival after anti-PD-1 treatment in patients with ccRCC (p value = 0.03; HR, 0.41; 95% CI, 0.18–0.92) (Figure 6D). Characteristics associated with anti-PD-1 treatment response in other types of cancer—including CD8$^+$ TIL counts, immune cell infiltration, and PD-L1 expression—were not associated with progression-free survival. This result was supported by *ex vivo* T cell assays performed using tumor single-cell suspensions from treatment-naive patients with ccRCC. The proportion of CD39$^+$ cells among CD8$^+$ TILs was significantly correlated with the restoration of IFN-γ and TNF-α production by *ex vivo* anti-PD-1 treatment (Figures S6A and S6B).

---

population. (H) Relative proportions of IFN-γ$^+$TNF$^+$ cells among CD39$^-$CD8$^+$ TILs (left) and CD39$^-$CD4$^+$ TILs (right) upon anti-CD3 stimulation in the presence or absence of eATP, iCD39, or iA2AR.

(I) Relative proportions of IFN-γ$^+$TNF$^+$ cells among CD8$^+$ TILs upon anti-CD3 stimulation with or without anti-PD-1-blocking antibody (aPD-1) and iA2AR (n = 18).

Data are represented as median with interquartile range; whiskers indicate the minimum and maximum values (A, B, and G).

Data are represented as mean ± SEM (C, D, E, and H).

*$p < 0.05$, **$p < 0.01$, ***$p < 0.001$, and ****$p < 0.0001$ by Mann-Whitney U test (A, B, D, E, G, and H), repeated measures ANOVA (C), and Wilcoxon matched-pairs signed-rank test (I).

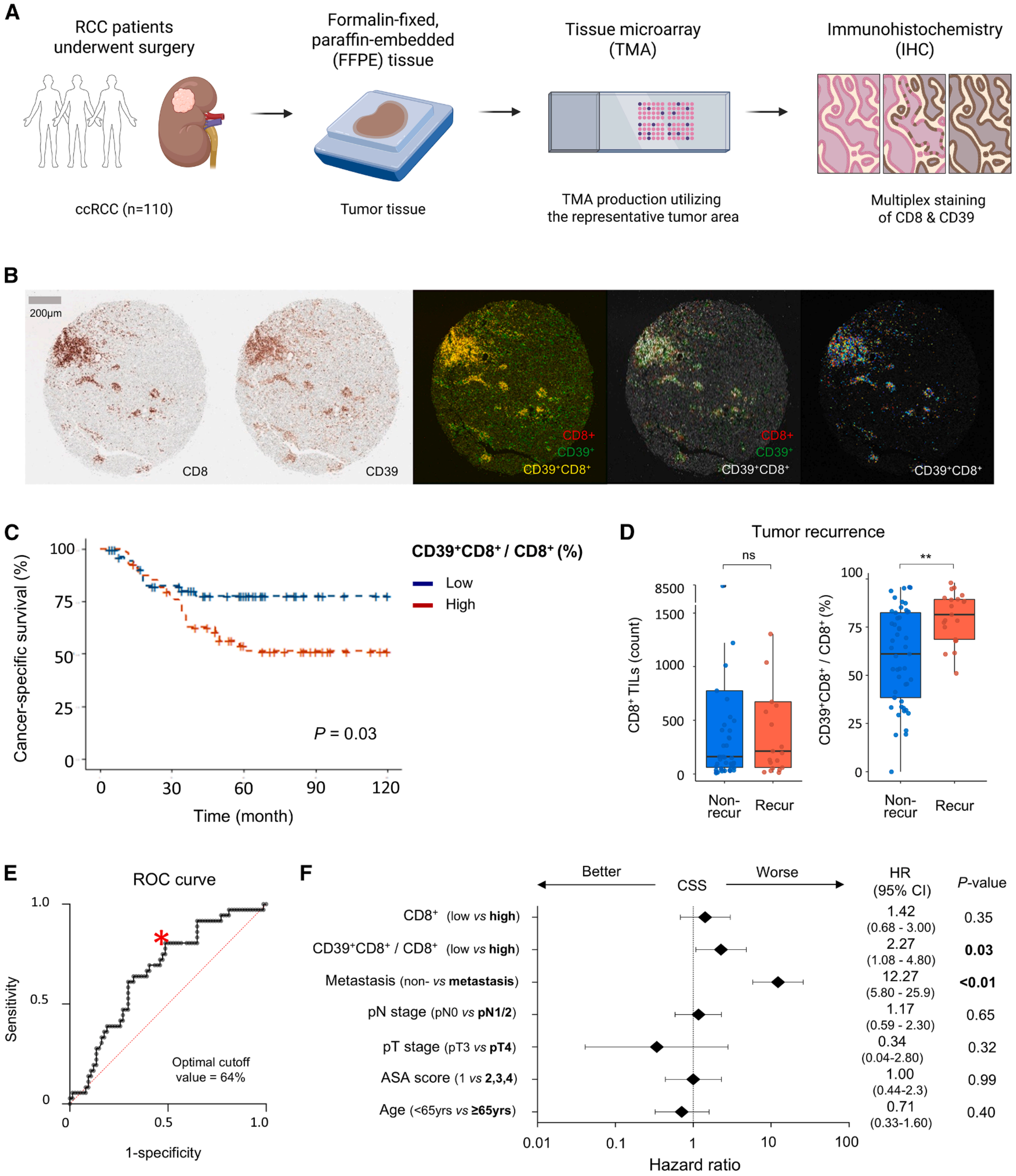

Figure 5. Enrichment of $CD39^+CD8^+$ TILs predicts poor prognosis of patients with ccRCC

(A) Experimental schematic of multiplex IHC (mIHC) staining of ccRCC tumors.

(B) Representative images of mIHC staining for CD8 and CD39 in the tumor field. Scale bars, 200 μm.

(C) Cancer-specific survival curves stratified according to the proportion of $CD39^+$ cells among $CD8^+$ TILs (*n* = 110). Patients were divided into low (*n* = 55) and high (*n* = 55) groups. *p* value was calculated by log rank test.

(D) Count of $CD8^+$ TILs (left) and proportion of $CD39^+$ cells among $CD8^+$ TILs (right), according to disease recurrence during follow-up. Non-recur, non-recurrence (*n* = 49); Recur, recurrence (*n* = 21).

(E) ROC curve for predicting cancer-specific survival using the proportion of $CD39^+$ cells among $CD8^+$ TILs. A red asterisk marks the optimal threshold.

(F) Forest plot of multivariate Cox regression analysis for cancer-specific survival (CSS) in patients with ccRCC. The group of $CD8^+$ TILs was stratified by its median value. The group of $CD39^+$ cells among $CD8^+$ TILs was stratified using the optimal cutoff value identified in (E). HR, hazard ratio; CSS, cancer-specific survival; CI, confidence interval.

Data are represented as median with interquartile range (D).

$^{**}p < 0.01$ by Mann-Whitney U test (D).

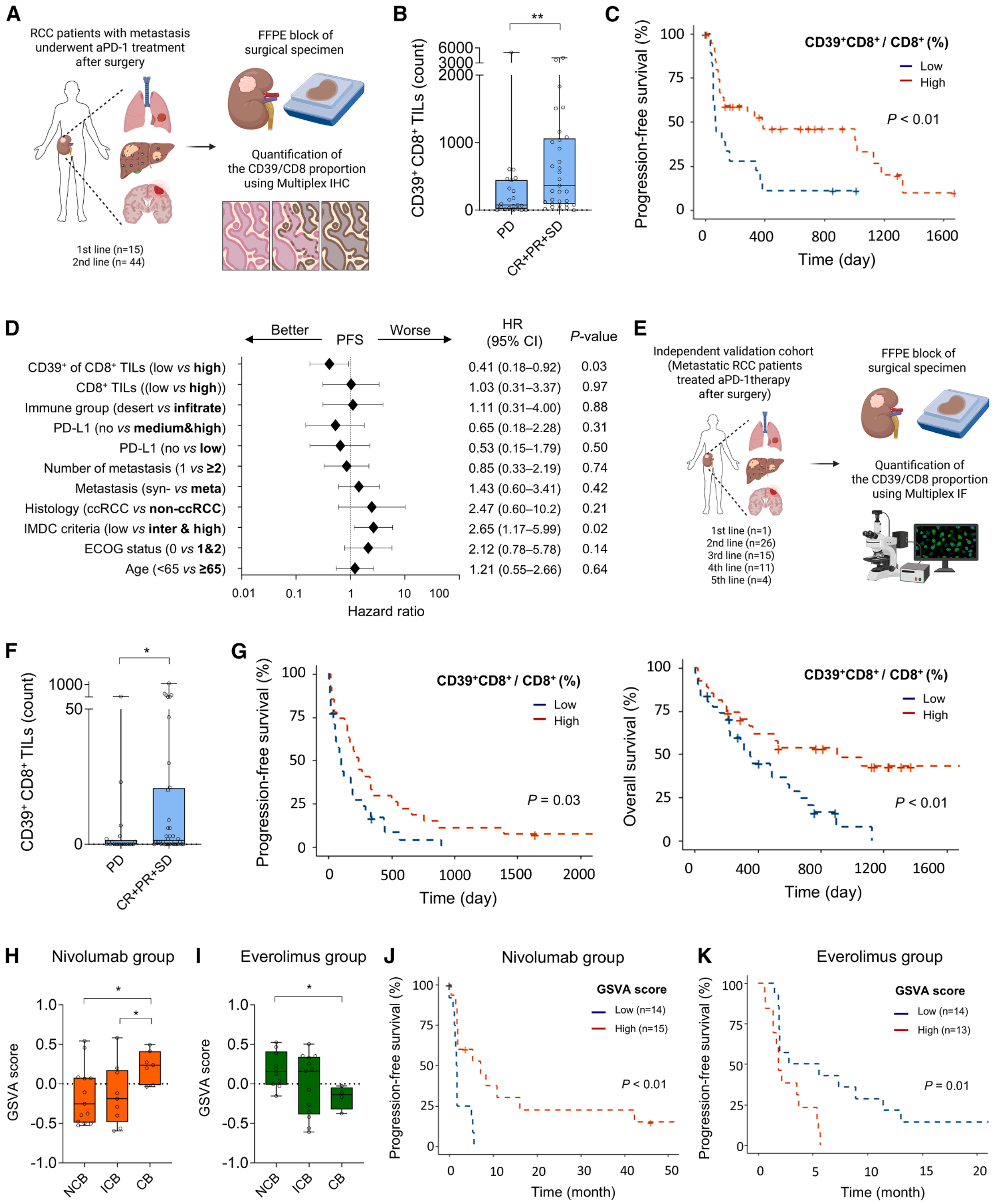

Figure 6. Enrichment of CD39$^+$CD8$^+$ TILs predicts favorable treatment responses to anti-PD-1 therapy

(A–D) mIHC-based evaluation of the association between CD39$^+$CD8$^+$ TIL abundance and prognosis following anti-PD-1 therapy (n = 59). (A) Experimental schematic of mIHC staining in patients with metastatic ccRCC undergoing anti-PD-1 blockade after surgery. (B) Count of CD39$^+$CD8$^+$ TILs according to the objective response to anti-PD-1 blockade: PD (n = 23) or CR + PR + SD (n = 33). (C) Kaplan-Meier curve for progression-free survival (PFS) of patients with metastatic ccRCC undergoing anti-PD-1 blockade. p value was calculated using log rank test. (D) Forest plot of multivariate Cox regression analysis for PFS in patients with metastatic ccRCC undergoing anti-PD-1 blockade.

(E–G) mIF-based evaluation of the association between CD39$^+$CD8$^+$ TIL abundance and prognosis following anti-PD-1 therapy in an independent cohort (n = 57). (E) Experimental schematic of mIF staining in patients with metastatic ccRCC undergoing anti-PD-1 blockade after surgery. (F) Count of CD39$^+$CD8$^+$ TILs according to the objective response to anti-PD-1 blockade: PD (n = 21) or CR + PR + SD (n = 36). (G) Kaplan-Meier curves for PFS (left) and overall survival (right) of patients with metastatic ccRCC undergoing anti-PD-1 blockade. p values were calculated using log rank test.

(legend continued on next page)

For an independent validation cohort of 57 patients with metastatic ccRCC who received anti-PD-1 therapy after surgery, the proportion of CD39$^+$ cells among CD8$^+$ TILs was quantified using multiplex immunofluorescence (mIF) on FFPE surgical specimens (Figure 6E; Table S7). Patients who achieved CR, PR, or SD exhibited a significantly higher count of CD39$^+$CD8$^+$ TILs compared to those with PD (Figure 6F). Based on an optimized cutoff value for the proportion of CD39$^+$ cells among CD8$^+$ TILs that maximized discriminatory power, patients were stratified into high- and low-CD39 groups. Kaplan-Meier analysis revealed that patients in the high-CD39 group experienced significantly prolonged progression-free survival and overall survival following anti-PD-1 treatment compared to those in the low-CD39 group (Figure 6G). Furthermore, multivariable Cox regression analysis confirmed that the high-CD39 group remained an independent prognostic factor for favorable clinical outcomes, including longer progression-free survival ($p = 0.046$; HR, 0.55; 95% CI, 0.30–0.99) and overall survival ($p = 0.017$; HR, 0.41; 95% CI, 0.20–0.85) (Figures S6C and S6D).

Analysis of a publicly available scRNA-seq dataset[31] supported the association between CD39$^+$CD8$^+$ T cell enrichment and therapeutic response, with higher proportions of CD39$^+$ PD-1$^+$ CD8$^+$ T cells observed in partial responders to immune checkpoint inhibitors (Figure S6E). We also validated the prognostic significance of CD39$^+$CD8$^+$ TIL enrichment using publicly available dataset from clinical trials (CheckMate 009, CheckMate 010, and CheckMate 025) involving anti-PD-1 (nivolumab) and mechanistic target of rapamycin (mTOR) inhibitor (everolimus) treatments in patients with ccRCC.[30] We first identified a gene set named "the CD39$^+$ T cell signature," which comprised 23 genes that were significantly upregulated in CD39$^+$ T cells compared to CD39$^-$ T cells in our scRNA-seq data (Table S8). We performed gene set variation analysis (GSVA) for the gene set of the CD39$^+$ T cell signature within the publicly available dataset from clinical trials. Patients who benefited from nivolumab treatment exhibited a significantly higher GSVA score for the CD39$^+$ T cell signature compared to patients with intermediate or no benefit among the International Metastatic Renal Cell Carcinoma Database Consortium (IMDC)-poor risk patients with an anticipated unfavorable prognosis (Figure 6H). On the other hand, patients who clinically benefited from everolimus treatment exhibited a significantly lower GSVA score for the CD39$^+$ T cell signature, compared to those with no benefit among IMDC-poor risk patients (Figure 6I). Furthermore, among IMDC-poor risk patients, individuals with higher scores for the CD39$^+$ T cell signature exhibited significantly improved progression-free survival upon nivolumab treatment but worse progression-free survival with everolimus treatment, compared to patients with lower scores for the CD39$^+$ T cell signature (Figures 6J and 6K). These findings indicated that among high-risk patients with ccRCC, CD39$^+$CD8$^+$ TILs predict favorable treatment responses to anti-PD-1 therapy but poor treatment responses to non-immune-based therapy, such as the mTOR inhibitor.

DISCUSSION

Here, we delineated the paradoxical prognostic significance of CD39$^+$CD8$^+$ TILs with regard to tumor recurrence and treatment responses to ICBs in ccRCC. Although CD39$^+$CD8$^+$ TIL enrichment predicted poor prognosis of patients, CD39$^+$CD8$^+$ TIL enrichment predicted favorable treatment responses to anti-PD-1 therapy. This paradoxical prognostic significance in ccRCC is explained by the dual properties of CD39$^+$CD8$^+$ TILs—tumor antigen specificity and immunosuppressive activity—which were demonstrated in the current study.

Previous studies have reported that CD39$^+$CD8$^+$ T cells are tumor-antigen-specific cells within tumors.[15–17,20,32] In many types of cancer other than ccRCC, CD39$^+$CD8$^+$ TIL enrichment has generally been considered a favorable marker for predicting recurrence-free survival or overall survival after surgery.[17,21,22] However, in ccRCC, CD39$^+$CD8$^+$ TIL enrichment exhibited the opposite prognostic association,[33,34] and the underlying mechanism has remained unclear. Our current study demonstrates that this opposite prognostic effect in ccRCC can be explained by the dual properties of CD39$^+$CD8$^+$ TILs.

We first observed CD39$^+$CD8$^+$ T cells among tumor-specific CD8$^+$ TILs and CAIX-specific CD8$^+$ TILs, showcasing terminally differentiated attributes. Moreover, CD39$^+$CD8$^+$ TILs exhibited enhanced TCR signaling, and their prevalence was correlated with a high mutational burden in the tumor. These findings suggested that the tumor-antigen-specific traits of CD39$^+$CD8$^+$ TILs may be intricately linked to the antigen specificity of each tumor, ultimately contributing to favorable responses to ICBs. However, CD39$^+$CD8$^+$ TILs also exert immunosuppressive activity via mechanisms dependent on ectonucleotidase activity and adenosine. CD39$^+$CD8$^+$ TILs exhibited augmented cAMP signaling as well as TCR signaling, and their enrichment was associated with a hypoxic tumor environment as well as a high mutational burden. Accordingly, the immunosuppressive nature of the tumor microenvironment can be strengthened by the enrichment of CD39$^+$CD8$^+$ TILs in the context of hypoxia, resulting in increased tumor recurrence.

Recently published evidence demonstrates the CD39-dependent immunosuppressive role of exhausted CD8$^+$ T cells in a mouse tumor model with hypoxia.[18] In contrast, CD39$^+$CD8$^+$ TILs have also shown prognostic significance in predicting better oncologic outcomes in breast cancer, head and neck cancer, hepatocellular carcinoma, and colorectal cancers.[17,21–23] This

---

(H and I) Gene set variation analysis (GSVA) scores for the CD39$^+$ T cell signature in RNA-seq data of tissue samples from clinical trials[30] of nivolumab ($n = 29$) (H) and everolimus ($n = 27$) (I) for IMDC-poor risk patients with ccRCC, according to clinical benefit. NCB, non-clinical benefit; ICB, intermediate clinical benefit; CB, clinical benefit.

(J and K) Progression-free survival of patients with metastatic ccRCC undergoing nivolumab ($n = 29$) (J) and everolimus ($n = 27$) (J) in clinical trials,[30] according to GSVA scores for the CD39$^+$ T cell signature in IMDC-poor risk patients with ccRCC. p values were calculated by log rank test.

Data are represented as median with interquartile range; whiskers indicate the minimum and maximum values (B, F, H, and I).

$^*p < 0.05$ and $^{**}p < 0.01$ by Mann-Whitney U test (B, I, and J).

raises doubts about whether the immunosuppressive role of CD39$^+$CD8$^+$ T cells realistically translates into an influence on human cancer prognosis. However, our present data indicated remarkable immunosuppressive activity of CD39$^+$CD8$^+$ TILs in hypoxic tumors. We focused our investigation on ccRCC—in which pseudohypoxic states can be induced even under minimal hypoxic or normoxic conditions, due to the overexpression of HIF molecules resulting from inactivating mutation of *VHL*. According to our data, 67% of patients with ccRCC exhibited non-synonymous *VHL* mutations (compared to 0% in other RCC subtypes), and 90.5% of patients exhibited *VHL* copy-number loss (compared to 30% in other RCC subtypes) (Figure 3F). Corroborating these distinct mutation profiles, ccRCC exhibited markedly higher proportions of CD39$^+$ cells among CD8$^+$ TILs (mean of 30%) and of CD8$^+$ T cells among CD39$^+$CD45$^+$ TILs (mean of 50%), compared to other RCC subtypes (means of <5% and <20%, respectively) (Figures 3A and 4B). Additionally, ccRCC tumors with elevated expression of hypoxic-related genes exhibited higher proportions of CD39$^+$ cells among CD8$^+$ TILs, compared to those with lower expression (Figures 3G and 3H). Accordingly, the levels of CD39$^+$CD8$^+$ TIL enrichment under a hypoxic environment can surpass those dictated solely by tumor antigenicity under a minimal hypoxic or normoxic environment, leading to exaggeration of the immunosuppressive role of CD39$^+$CD8$^+$ TILs under hypoxic conditions. Further studies are warranted to examine whether the immunosuppressive roles of CD39$^+$CD8$^+$ TILs are prominent in other human tumors that exhibit high levels of hypoxia, in addition to ccRCC.

Our findings make several implications regarding therapeutic strategies for patients with ccRCC. As anti-PD-1-based treatments are becoming standard of care in advanced or metastatic ccRCC,[35,36] there have been continuous efforts to find effective biomarkers to predict responses to anti-PD-1 treatment. However, several characteristics associated with anti-PD-1 treatment response in other types of cancer—including CD8$^+$ T cell infiltration, PD-L1 expression, TMB, and fsINDEL—have failed to demonstrate predictive value or have shown inconsistent findings in ccRCC.[30,37,38] Here, we showed that an IHC-based predictive biomarker, the proportion of CD39$^+$CD8$^+$ T cells, successfully predicted anti-PD-1 treatment response better than previously suggested biomarkers, including immune group, T cell infiltration, and PD-L1 expression (Figure 6D). Additionally, although patients with ccRCC with high levels of CD39$^+$CD8$^+$ TILs are predicted to face a poor prognosis, they may be more likely to derive therapeutic benefits from anti-PD-1 treatment. Moreover, the efficacy of anti-PD-1 treatment in these patients could be leveraged by modulating CD39-mediated immunosuppressive activity—for example, through the use of A2AR inhibitors[10] or CD39 inhibitors.[39] A detailed understanding of CD39$^+$CD8$^+$ TILs will provide insights for therapeutic strategies, as well as prognostic biomarkers for the management of patients with ccRCC and other types of hypoxic tumors.

Limitations of the study

Despite the comprehensive nature of our analyses, several limitations should be acknowledged. First, the use of patient-derived samples poses inherent limitations, as the heterogeneity in genetic background, TMB, and immune microenvironment may confound the interpretation of the results. Although we attempted to mitigate this through consistent experimental procedures and integrated multi-modal analysis, further validation in larger, more homogeneous cohorts would strengthen our findings. Second, the *in vitro* functional assays conducted in this study may not fully recapitulate the complexity of the *in vivo* tumor microenvironment. In particular, the spatial context and dynamic interactions among various immune, tumor, and stromal cells may significantly influence CD39$^+$CD8$^+$ T cell behavior. Future studies incorporating spatial multi-omics or *in vivo* models will be needed to validate our findings. Third, assays for rapid expansion of CD8$^+$ T cells and identification of tumor-reactive CD8$^+$ T cells based on 4-1BB upregulation following co-culture with autologous tumor cells require further validation. For example, co-culture with EPCAM$^-$ cells could be included as a negative control in addition to co-culture with EPCAM$^+$ cells. Fourth, although we aimed to elucidate the mechanism underlying CD39 expression in CD8$^+$ T cells, we were unable to fully determine the precise molecular pathways. While our correlation analysis suggests a potential role of hypoxia in driving CD39 expression, it does not establish a causal relationship. Moreover, although the pseudotime analysis implicates a potential role for CREM, the inherent limitations of this approach preclude definitive clarification of CREM's exact function in the expression of CD39.

RESOURCE AVAILABILITY

Lead contact

Requests for further information should be directed to and will be fulfilled by the lead contact, Prof. Eui-Cheol Shin (ecshin@kaist.ac.kr).

Materials availability

Further information and requests for resources and reagents should be directed to and will be fulfilled by the lead contact, Prof. Eui-Cheol Shin (ecshin@kaist.ac.kr).

Data and code availability

- Single-cell sequencing data have been deposited on the Gene Expression Omnibus under the accession number GEO: GSE285701 and are publicly available.
- Raw data for whole-exome sequencing of all samples have been deposited on the NCBI's Sequence Read Archive, under BioProject PRJNA1200786.
- Whole-transcriptome sequencing (WTS) data are provided in Table S9.
- Codes for sequencing analyses have been deposited at https://github.com/code-data-upload/RCC_CD39.
- Any additional information required to reanalyze the data reported in this article is available from the lead contact on request.

ACKNOWLEDGMENTS

This work was supported by the Bio & Medical Technology Development Program (RS-2024-00439160; E.-C.S.) through the National Research Foundation of Korea (NRF), funded by the Ministry of Science and ICT (MSIT). This study was also supported by a grant (RS-2023-00248383; Y.J.L.) and a Global PhD Fellowship (NRF-2018H1A2A1063212; Y.J.L.) from the NRF, also funded by the MSIT. Multiplex immunofluorescence staining was supported by the Gyeonggido Business and Science Accelerator (GBSA).

AUTHOR CONTRIBUTIONS

Y.J.L., S.H.J., J.H.J., H.N., M. Jeon, E.-S.K., J.Y.J., C.-H.K., K.Y.C., J.Y.L., S. H., J.Y.K., S.-I.K., J.-H.C., C.G.K., S.J.S., M.K., and S.I.S. were involved in sample acquisition. Y.J.L., S.H.J., J.H.Y., S.-j.B., J.H.J., H.N., M. Jeon, and E.-S.K. were involved in data acquisition and analysis. Y.J.L., S.-H.P., M. Jung, M.K., S.I.S., and E.-C.S. were involved in data interpretation and discussion of results. Y.J.L., S.-j.B., M.K., S.I.S., and E.-C.S. contributed to the conceptual design of the study. Y.J.L., S.H.J., J.H.Y., M. Jung, and E.-C.S. wrote the manuscript.

DECLARATION OF INTERESTS

The authors declare no competing interests.

DECLARATION OF GENERATIVE AI AND AI-ASSISTED TECHNOLOGIES IN THE WRITING PROCESS

During the preparation of this work, the authors used ChatGPT for English language editing of the manuscript. After using this tool, the authors reviewed and edited the content as needed and take full responsibility for the content of the publication.

STAR★METHODS

Detailed methods are provided in the online version of this paper and include the following:

- KEY RESOURCES TABLE
- EXPERIMENTAL MODEL AND STUDY PARTICIPANT DETAILS
  - Human specimens
- METHOD DETAILS
  - Single cell collection
  - Flow cytometry
  - Single-cell library preparation
  - Single-cell sequencing data processing
  - Single-cell sequencing clustering and annotation
  - Single-cell surface protein expression analysis
  - Tumor-specificity verification of $CD8^+$ T cells
  - Bulk TCR-sequencing and analysis
  - Single-cell TCR repertoire analysis
  - Pseudotime analysis
  - Whole exome sequencing analysis
  - Bulk RNA-sequencing and analysis
  - TCGA data analysis
  - Functional capacity evaluation of $CD8^+$ TILs
  - *In vitro* functional restoration assay
  - Immunohistochemical stains and analysis
  - Multiplex immunofluorescence staining and analysis
  - Stimulation of naive $CD8^+$ T cells
  - Quantification of ATP and adenosine
  - Quantification of intracellular cAMP
  - *In vitro* suppression assay
  - Functional assay in CD39-depleted environment
- QUANTIFICATION AND STATISTICAL ANALYSIS

SUPPLEMENTAL INFORMATION

Supplemental information can be found online at https://doi.org/10.1016/j.xcrm.2025.102360.

Received: September 24, 2024
Revised: June 30, 2025
Accepted: August 21, 2025
Published: September 16, 2025

REFERENCES

1. Jing, X., Yang, F., Shao, C., Wei, K., Xie, M., Shen, H., and Shu, Y. (2019). Role of hypoxia in cancer therapy by regulating the tumor microenvironment. Mol. Cancer *18*, 157. https://doi.org/10.1186/s12943-019-1089-9.
2. Jayaprakash, P., Vignali, P.D.A., Delgoffe, G.M., and Curran, M.A. (2022). Hypoxia Reduction Sensitizes Refractory Cancers to Immunotherapy. Annu. Rev. Med. *73*, 251–265. https://doi.org/10.1146/annurev-med-060619-022830.
3. McGettrick, A.F., and O'Neill, L.A.J. (2020). The Role of HIF in Immunity and Inflammation. Cell Metab. *32*, 524–536. https://doi.org/10.1016/j.cmet.2020.08.002.
4. Wu, Q., You, L., Nepovimova, E., Heger, Z., Wu, W., Kuca, K., and Adam, V. (2022). Hypoxia-inducible factors: master regulators of hypoxic tumor immune escape. J. Hematol. Oncol. *15*, 77. https://doi.org/10.1186/s13045-022-01292-6.
5. Hsieh, J.J., Purdue, M.P., Signoretti, S., Swanton, C., Albiges, L., Schmidinger, M., Heng, D.Y., Larkin, J., and Ficarra, V. (2017). Renal cell carcinoma. Nat. Rev. Dis. Primers *3*, 17009. https://doi.org/10.1038/nrdp.2017.9.
6. Vuong, L., Kotecha, R.R., Voss, M.H., and Hakimi, A.A. (2019). Tumor Microenvironment Dynamics in Clear-Cell Renal Cell Carcinoma. Cancer Discov. *9*, 1349–1357. https://doi.org/10.1158/2159-8290.Cd-19-0499.
7. Klatte, T., Seligson, D.B., Riggs, S.B., Leppert, J.T., Berkman, M.K., Kleid, M.D., Yu, H., Kabbinavar, F.F., Pantuck, A.J., and Belldegrun, A.S. (2007). Hypoxia-inducible factor 1 alpha in clear cell renal cell carcinoma. Clin. Cancer Res. *13*, 7388–7393. https://doi.org/10.1158/1078-0432.Ccr-07-0411.
8. Choueiri, T.K., and Kaelin, W.G., Jr. (2020). Targeting the HIF2-VEGF axis in renal cell carcinoma. Nat. Med. *26*, 1519–1530. https://doi.org/10.1038/s41591-020-1093-z.
9. Sidders, B., Zhang, P., Goodwin, K., O'Connor, G., Russell, D.L., Borodovsky, A., Armenia, J., McEwen, R., Linghu, B., Bendell, J.C., et al. (2020). Adenosine Signaling Is Prognostic for Cancer Outcome and Has Predictive Utility for Immunotherapeutic Response. Clin. Cancer Res. *26*, 2176–2187. https://doi.org/10.1158/1078-0432.Ccr-19-2183.
10. Fong, L., Hotson, A., Powderly, J.D., Sznol, M., Heist, R.S., Choueiri, T.K., George, S., Hughes, B.G.M., Hellmann, M.D., Shepard, D.R., et al. (2020). Adenosine 2A Receptor Blockade as an Immunotherapy for Treatment-Refractory Renal Cell Cancer. Cancer Discov. *10*, 40–53. https://doi.org/10.1158/2159-8290.Cd-19-0980.
11. Braun, D.A., Bakouny, Z., Hirsch, L., Flippot, R., Van Allen, E.M., Wu, C.J., and Choueiri, T.K. (2021). Beyond conventional immune-checkpoint inhibition - novel immunotherapies for renal cell carcinoma. Nat. Rev. Clin. Oncol. *18*, 199–214. https://doi.org/10.1038/s41571-020-00455-z.
12. Giraldo, N.A., Becht, E., Vano, Y., Petitprez, F., Lacroix, L., Validire, P., Sanchez-Salas, R., Ingels, A., Oudard, S., Moatti, A., et al. (2017). Tumor-Infiltrating and Peripheral Blood T-cell Immunophenotypes Predict Early Relapse in Localized Clear Cell Renal Cell Carcinoma. Clin. Cancer Res. *23*, 4416–4428. https://doi.org/10.1158/1078-0432.Ccr-16-2848.
13. Fridman, W.H., Zitvogel, L., Sautès-Fridman, C., and Kroemer, G. (2017). The immune contexture in cancer prognosis and treatment. Nat. Rev. Clin. Oncol. *14*, 717–734. https://doi.org/10.1038/nrclinonc.2017.101.
14. Su, S., Akbarinejad, S., and Shahriyari, L. (2021). Immune classification of clear cell renal cell carcinoma. Sci. Rep. *11*, 4338. https://doi.org/10.1038/s41598-021-83767-z.
15. Canale, F.P., Ramello, M.C., Núñez, N., Araujo Furlan, C.L., Bossio, S.N., Gorosito Serrán, M., Tosello Boari, J., Del Castillo, A., Ledesma, M., Sedlik, C., et al. (2018). CD39 Expression Defines Cell Exhaustion in Tumor-Infiltrating CD8(+) T Cells. Cancer Res. *78*, 115–128. https://doi.org/10.1158/0008-5472.Can-16-2684.
16. Simoni, Y., Becht, E., Fehlings, M., Loh, C.Y., Koo, S.L., Teng, K.W.W., Yeong, J.P.S., Nahar, R., Zhang, T., Kared, H., et al. (2018). Bystander

CD8(+) T cells are abundant and phenotypically distinct in human tumour infiltrates. Nature *557*, 575–579. https://doi.org/10.1038/s41586-018-0130-2.

17. Duhen, T., Duhen, R., Montler, R., Moses, J., Moudgil, T., de Miranda, N. F., Goodall, C.P., Blair, T.C., Fox, B.A., McDermott, J.E., et al. (2018). Co--expression of CD39 and CD103 identifies tumor-reactive CD8 T cells in human solid tumors. Nat. Commun. *9*, 2724. https://doi.org/10.1038/s41467-018-05072-0.

18. Vignali, P.D.A., DePeaux, K., Watson, M.J., Ye, C., Ford, B.R., Lontos, K., McGaa, N.K., Scharping, N.E., Menk, A.V., Robson, S.C., et al. (2023). Hypoxia drives CD39-dependent suppressor function in exhausted T cells to limit antitumor immunity. Nat. Immunol. *24*, 267–279. https://doi.org/10.1038/s41590-022-01379-9.

19. Yeong, J., Suteja, L., Simoni, Y., Lau, K.W., Tan, A.C., Li, H.H., Lim, S., Loh, J.H., Wee, F.Y.T., Nerurkar, S.N., et al. (2021). Intratumoral CD39(+) CD8(+) T Cells Predict Response to Programmed Cell Death Protein-1 or Programmed Death Ligand-1 Blockade in Patients With NSCLC. J. Thorac. Oncol. *16*, 1349–1358. https://doi.org/10.1016/j.jtho.2021.04.016.

20. Chow, A., Uddin, F.Z., Liu, M., Dobrin, A., Nabet, B.Y., Mangarin, L., Lavin, Y., Rizvi, H., Tischfield, S.E., Quintanal-Villalonga, A., et al. (2023). The ectonucleotidase CD39 identifies tumor-reactive CD8(+) T cells predictive of immune checkpoint blockade efficacy in human lung cancer. Immunity *56*, 93–106.e6. https://doi.org/10.1016/j.immuni.2022.12.001.

21. Lee, Y.J., Kim, J.Y., Jeon, S.H., Nam, H., Jung, J.H., Jeon, M., Kim, E.S., Bae, S.J., Ahn, J., Yoo, T.K., et al. (2022). CD39(+) tissue-resident memory CD8(+) T cells with a clonal overlap across compartments mediate antitumor immunity in breast cancer. Sci. Immunol. *7*, eabn8390. https://doi.org/10.1126/sciimmunol.abn8390.

22. Liu, T., Tan, J., Wu, M., Fan, W., Wei, J., Zhu, B., Guo, J., Wang, S., Zhou, P., Zhang, H., et al. (2021). High-affinity neoantigens correlate with better prognosis and trigger potent antihepatocellular carcinoma (HCC) activity by activating CD39(+)CD8(+) T cells. Gut *70*, 1965–1977. https://doi.org/10.1136/gutjnl-2020-322196.

23. Talhouni, S., Fadhil, W., Mongan, N.P., Field, L., Hunter, K., Makhsous, S., Maciel-Guerra, A., Kaur, N., Nestarenkaite, A., Laurinavicius, A., et al. (2023). Activated tissue resident memory T-cells (CD8+CD103+CD39+) uniquely predict survival in left sided "immune-hot" colorectal cancers. Front. Immunol. *14*, 1057292. https://doi.org/10.3389/fimmu.2023.1057292.

24. Krishna, C., DiNatale, R.G., Kuo, F., Srivastava, R.M., Vuong, L., Chowell, D., Gupta, S., Vanderbilt, C., Purohit, T.A., Liu, M., et al. (2021). Single-cell sequencing links multiregional immune landscapes and tissue-resident T cells in ccRCC to tumor topology and therapy efficacy. Cancer Cell *39*, 662–677.e6. https://doi.org/10.1016/j.ccell.2021.03.007.

25. Ditte, P., Dequiedt, F., Svastova, E., Hulikova, A., Ohradanova-Repic, A., Zatovicova, M., Csaderova, L., Kopacek, J., Supuran, C.T., Pastorekova, S., and Pastorek, J. (2011). Phosphorylation of carbonic anhydrase IX controls its ability to mediate extracellular acidification in hypoxic tumors. Cancer Res. *71*, 7558–7567. https://doi.org/10.1158/0008-5472.Can-11-2520.

26. Pradhan, A., Avelar, G.M., Bain, J.M., Childers, D.S., Larcombe, D.E., Netea, M.G., Shekhova, E., Munro, C.A., Brown, G.D., Erwig, L.P., et al. (2018). Hypoxia Promotes Immune Evasion by Triggering β-Glucan Masking on the Candida albicans Cell Surface via Mitochondrial and cAMP-Protein Kinase A Signaling. mBio *9*, e01318-18. https://doi.org/10.1128/mBio.01318-18.

27. Simko, V., Iuliano, F., Sevcikova, A., Labudova, M., Barathova, M., Radvak, P., Pastorekova, S., Pastorek, J., and Csaderova, L. (2017). Hypoxia induces cancer-associated cAMP/PKA signalling through HIF-mediated transcriptional control of adenylyl cyclases VI and VII. Sci. Rep. *7*, 10121. https://doi.org/10.1038/s41598-017-09549-8.

28. Vignali, D.A.A., Collison, L.W., and Workman, C.J. (2008). How regulatory T cells work. Nat. Rev. Immunol. *8*, 523–532. https://doi.org/10.1038/nri2343.

29. Ohta, A., and Sitkovsky, M. (2014). Extracellular adenosine-mediated modulation of regulatory T cells. Front. Immunol. *5*, 304. https://doi.org/10.3389/fimmu.2014.00304.

30. Braun, D.A., Hou, Y., Bakouny, Z., Ficial, M., Sant' Angelo, M., Forman, J., Ross-Macdonald, P., Berger, A.C., Jegede, O.A., Elagina, L., et al. (2020). Interplay of somatic alterations and immune infiltration modulates response to PD-1 blockade in advanced clear cell renal cell carcinoma. Nat. Med. *26*, 909–918. https://doi.org/10.1038/s41591-020-0839-y.

31. Bi, K., He, M.X., Bakouny, Z., Kanodia, A., Napolitano, S., Wu, J., Grimaldi, G., Braun, D.A., Cuoco, M.S., Mayorga, A., et al. (2021). Tumor and immune reprogramming during immunotherapy in advanced renal cell carcinoma. Cancer Cell *39*, 649–661.e5. https://doi.org/10.1016/j.ccell.2021.02.015.

32. Kortekaas, K.E., Santegoets, S.J., Sturm, G., Ehsan, I., van Egmond, S.L., Finotello, F., Trajanoski, Z., Welters, M.J.P., van Poelgeest, M.I.E., and van der Burg, S.H. (2020). CD39 Identifies the CD4(+) Tumor-Specific T-cell Population in Human Cancer. Cancer Immunol. Res. *8*, 1311–1321. https://doi.org/10.1158/2326-6066.Cir-20-0270.

33. Qi, Y., Xia, Y., Lin, Z., Qu, Y., Qi, Y., Chen, Y., Zhou, Q., Zeng, H., Wang, J., Chang, Y., et al. (2020). Tumor-infiltrating CD39(+)CD8(+) T cells determine poor prognosis and immune evasion in clear cell renal cell carcinoma patients. Cancer Immunol. Immunother. *69*, 1565–1576. https://doi.org/10.1007/s00262-020-02563-2.

34. Annels, N.E., Denyer, M., Nicol, D., Hazell, S., Silvanto, A., Crockett, M., Hussain, M., Moller-Levet, C., and Pandha, H. (2023). The dysfunctional immune response in renal cell carcinoma correlates with changes in the metabolic landscape of ccRCC during disease progression. Cancer Immunol. Immunother. *72*, 4221–4234. https://doi.org/10.1007/s00262-023-03558-5.

35. Motzer, R., Alekseev, B., Rha, S.Y., Porta, C., Eto, M., Powles, T., Grünwald, V., Hutson, T.E., Kopyltsov, E., Méndez-Vidal, M.J., et al. (2021). Lenvatinib plus Pembrolizumab or Everolimus for Advanced Renal Cell Carcinoma. N. Engl. J. Med. *384*, 1289–1300. https://doi.org/10.1056/NEJMoa2035716.

36. Choueiri, T.K., Tomczak, P., Park, S.H., Venugopal, B., Ferguson, T., Symeonides, S.N., Hajek, J., Chang, Y.H., Lee, J.L., Sarwar, N., et al. (2024). Overall Survival with Adjuvant Pembrolizumab in Renal-Cell Carcinoma. N. Engl. J. Med. *390*, 1359–1371. https://doi.org/10.1056/NEJMoa2312695.

37. Au, L., Hatipoglu, E., Robert de Massy, M., Litchfield, K., Beattie, G., Rowan, A., Schnidrig, D., Thompson, R., Byrne, F., Horswell, S., et al. (2021). Determinants of anti-PD-1 response and resistance in clear cell renal cell carcinoma. Cancer Cell *39*, 1497–1518.e11. https://doi.org/10.1016/j.ccell.2021.10.001.

38. Carretero-González, A., Lora, D., Martín Sobrino, I., Sáez Sanz, I., Bourlon, M.T., Anido Herranz, U., Martínez Chanzá, N., Castellano, D., and de Velasco, G. (2020). The Value of PD-L1 Expression as Predictive Biomarker in Metastatic Renal Cell Carcinoma Patients: A Meta-Analysis of Randomized Clinical Trials. Cancers (Basel) *12*. https://doi.org/10.3390/cancers12071945.

39. Li, X.Y., Moesta, A.K., Xiao, C., Nakamura, K., Casey, M., Zhang, H., Madore, J., Lepletier, A., Aguilera, A.R., Sundarrajan, A., et al. (2019). Targeting CD39 in Cancer Reveals an Extracellular ATP- and Inflammasome-Driven Tumor Immunity. Cancer Discov. *9*, 1754–1773. https://doi.org/10.1158/2159-8290.Cd-19-0541.

40. Hao, Y., Hao, S., Andersen-Nissen, E., Mauck, W.M., 3rd, Zheng, S., Butler, A., Lee, M.J., Wilk, A.J., Darby, C., Zager, M., et al. (2021). Integrated analysis of multimodal single-cell data. Cell *184*, 3573–3587.e29. https://doi.org/10.1016/j.cell.2021.04.048.

41. Korsunsky, I., Millard, N., Fan, J., Slowikowski, K., Zhang, F., Wei, K., Baglaenko, Y., Brenner, M., Loh, P.R., and Raychaudhuri, S. (2019). Fast,

sensitive and accurate integration of single-cell data with Harmony. Nat. Methods *16*, 1289–1296. https://doi.org/10.1038/s41592-019-0619-0.

42. Li, K., Tandurella, J.A., Gai, J., Zhu, Q., Lim, S.J., Thomas, D.L., 2nd, Xia, T., Mo, G., Mitchell, J.T., Montagne, J., et al. (2022). Multi-omic analyses of changes in the tumor microenvironment of pancreatic adenocarcinoma following neoadjuvant treatment with anti-PD-1 therapy. Cancer Cell *40*, 1374–1391.e7. https://doi.org/10.1016/j.ccell.2022.10.001.

43. Thommen, D.S., Koelzer, V.H., Herzig, P., Roller, A., Trefny, M., Dimeloe, S., Kiialainen, A., Hanhart, J., Schill, C., Hess, C., et al. (2018). A transcriptionally and functionally distinct PD-1(+) CD8(+) T cell pool with predictive potential in non-small-cell lung cancer treated with PD-1 blockade. Nat. Med. *24*, 994–1004. https://doi.org/10.1038/s41591-018-0057-z.

44. Bolotin, D.A., Poslavsky, S., Mitrophanov, I., Shugay, M., Mamedov, I.Z., Putintseva, E.V., and Chudakov, D.M. (2015). MiXCR: software for comprehensive adaptive immunity profiling. Nat. Methods *12*, 380–381. https://doi.org/10.1038/nmeth.3364.

45. Goncharov, M., Bagaev, D., Shcherbinin, D., Zvyagin, I., Bolotin, D., Thomas, P.G., Minervina, A.A., Pogorelyy, M.V., Ladell, K., McLaren, J. E., et al. (2022). VDJdb in the pandemic era: a compendium of T cell receptors specific for SARS-CoV-2. Nat. Methods *19*, 1017–1019. https://doi.org/10.1038/s41592-022-01578-0.

46. Szolek, A., Schubert, B., Mohr, C., Sturm, M., Feldhahn, M., and Kohlbacher, O. (2014). OptiType: precision HLA typing from next-generation sequencing data. Bioinformatics *30*, 3310–3316. https://doi.org/10.1093/bioinformatics/btu548.

47. Qiu, X., Hill, A., Packer, J., Lin, D., Ma, Y.A., and Trapnell, C. (2017). Single-cell mRNA quantification and differential analysis with Census. Nat. Methods *14*, 309–315. https://doi.org/10.1038/nmeth.4150.

48. Li, H., van der Leun, A.M., Yofe, I., Lubling, Y., Gelbard-Solodkin, D., van Akkooi, A.C.J., van den Braber, M., Rozeman, E.A., Haanen, J.B.A.G., Blank, C.U., et al. (2019). Dysfunctional CD8 T Cells Form a Proliferative, Dynamically Regulated Compartment within Human Melanoma. Cell *176*, 775–789.e18. https://doi.org/10.1016/j.cell.2018.11.043.

49. Mermel, C.H., Schumacher, S.E., Hill, B., Meyerson, M.L., Beroukhim, R., and Getz, G. (2011). GISTIC2.0 facilitates sensitive and confident localization of the targets of focal somatic copy-number alteration in human cancers. Genome Biol. *12*, R41. https://doi.org/10.1186/gb-2011-12-4-r41.

50. Love, M.I., Huber, W., and Anders, S. (2014). Moderated estimation of fold change and dispersion for RNA-seq data with DESeq2. Genome Biol. *15*, 550. https://doi.org/10.1186/s13059-014-0550-8.

51. Hänzelmann, S., Castelo, R., and Guinney, J. (2013). GSVA: gene set variation analysis for microarray and RNA-seq data. BMC Bioinf. *14*. https://doi.org/10.1186/1471-2105-14-7.

52. Tsujikawa, T., Kumar, S., Borkar, R.N., Azimi, V., Thibault, G., Chang, Y.H., Balter, A., Kawashima, R., Choe, G., Sauer, D., et al. (2017). Quantitative Multiplex Immunohistochemistry Reveals Myeloid-Inflamed Tumor-Immune Complexity Associated with Poor Prognosis. Cell Rep. *19*, 203–217. https://doi.org/10.1016/j.celrep.2017.03.037.

53. McQuin, C., Goodman, A., Chernyshev, V., Kamentsky, L., Cimini, B.A., Karhohs, K.W., Doan, M., Ding, L., Rafelski, S.M., Thirstrup, D., et al. (2018). CellProfiler 3.0: Next-generation image processing for biology. PLoS Biol. *16*, e2005970. https://doi.org/10.1371/journal.pbio.2005970.

STAR★METHODS

KEY RESOURCES TABLE

REAGENT or RESOURCE	SOURCE	IDENTIFIER
Antibodies		
BV510 anti-human CD3 antibody (clone UCHT1)	BD Biosciences	Cat#: 563109; RRID: AB_2732053
APC-Cy7 anti-human CD3 antibody (clone SK7)	BD Biosciences	Cat#: 557832; RRID: AB_396890
PerCP anti-human CD3 antibody (clone SP34-2)	BD Biosciences	Cat#: 552851; RRID: AB_394492
PerCP-Cy5.5 anti-human CD4 antibody (clone RPA-T4)	BD Biosciences	Cat#: 560650; RRID: AB_1727476
BV786 anti-human CD4 antibody (clone SK3)	BD Biosciences	Cat#: 563877; RRID: AB_2738462
PE-Cy7 anti-human CD4 antibody (clone SK3)	BD Biosciences	Cat#: 557852; RRID: AB_396897
APC-H7 anti-human CD8 antibody (clone SK1)	BD Biosciences	Cat#: 560179; RRID: AB_1645481
Alexa Fluor 700 anti-human CD8 antibody (clone RPA-T8)	BD Biosciences	Cat#: 557945; RRID: AB_396953
PE-Cy7 anti-human CD8 antibody (clone RPA-T8)	BD Biosciences	Cat#: 557746; RRID: AB_396852
BV711 anti-human CD8 antibody (clone RPA-T8)	BD Biosciences	Cat#: 563677; RRID: AB_2744463
PE-CF594 anti-human CD14 antibody (clone MφP9)	BD Biosciences	Cat#: 562335; RRID: AB_11153663
PE-Cy7 anti-human CD14 antibody (clone MφP9)	BD Biosciences	Cat#: 562698; RRID: AB_2737729
PE-CF594 anti-human CD19 antibody (clone HIB19)	BD Biosciences	Cat#: 562294; RRID: AB_11154408
BV786 anti-human CD56 antibody (clone NCAM16.2)	BD Biosciences	Cat#: 564058; RRID: AB_2738569
Alexa Fluor 700 anti-human CD45 antibody (clone HI30)	BD Biosciences	Cat#: 560566; RRID: AB_1645452
APC anti-human CD137 antibody (clone 4B4-1)	BD Biosciences	Cat#: 550890; RRID: AB_398477
Alexa Fluor 700 anti-human TNF antibody (clone Mab11)	BD Biosciences	Cat#: 557996; RRID: AB_396978
PE-Cy7 anti-human IFN-γ antibody (clone 4S.B3)	BD Biosciences	Cat#: 557844; RRID: AB_396894
BV421 anti-human IFN-γ antibody (clone 4S.B3)	BD Biosciences	Cat#: 564791; RRID: AB_2738952
BV711 anti-human IFN-γ antibody (clone B27)	BD Biosciences	Cat#: 564039; RRID: AB_2738557
PE-Cy7 anti-human CD127 antibody (clone HIL-7R-M21)	BD Biosciences	Cat#: 560822; RRID: AB_2033938
BV650 anti-human CD25 antibody (clone M-A251)	BD Biosciences	Cat#: 563719; RRID: AB_2744337
BB515 anti-human CD39 antibody (clone Tü66)	BD Biosciences	Cat#: 565469; RRID: AB_2722754
BV711 anti-human CD39 antibody (clone Tü66)	BD Biosciences	Cat#: 563680; RRID: AB_2738369
PE anti-human CD39 antibody (clone Tü66)	BD Biosciences	Cat#: 555464; RRID: AB_395856
BV605 anti-human CD3 antibody (clone OKT3)	BioLegend	Cat#: 317322; RRID: AB_2563871
APC anti-human CD3 antibody (clone HIT3a)	BioLegend	Cat#: 300312; RRID: AB_314054
FITC anti-human CD8 antibody (clone RPA-T8)	BioLegend	Cat#: 301050; RRID: AB_314146
APC anti-human CD8 antibody (clone SK1)	BioLegend	Cat#: 344722; RRID: AB_2563873
PE-Cy7 anti-human TCRγ/δ antibody (clone B1)	BioLegend	Cat#: 331222; RRID: AB_2563874
BV785 anti-human CD326 antibody (clone 9C4)	BioLegend	Cat#: 324238; RRID: AB_2563875
PE-Cy7 anti-human TCR Vα7.2 antibody (clone 3C10)	BioLegend	Cat#: 351712; RRID: AB_2563876
APC-Cy7 anti-human CD45 antibody (clone HI30)	BioLegend	Cat#: 304014; RRID: AB_2563877
PE-Cy7 anti-human CD56 antibody (clone HCD56)	BioLegend	Cat#: 318318; RRID: AB_604107
PE anti-human CD137 antibody (clone 4B4-1)	BioLegend	Cat#: 309804; RRID: AB_2563878
BV510 anti-human Ki-67 antibody (clone Ki-67)	BioLegend	Cat#: 350518; RRID: AB_2563879
BV605 anti-human Ki-67 antibody (clone Ki-67)	BioLegend	Cat#: 350522; RRID: AB_2563880
BV711 anti-human Ki-67 antibody (clone Ki-67)	BioLegend	Cat#: 350516; RRID: AB_2563881
APC-Cy7 anti-human CD45RA antibody (clone HI100)	BioLegend	Cat#: 304128; RRID: AB_2563882
BV421 anti-human CD39 antibody (clone A1)	BioLegend	Cat#: 328214; RRID: AB_2563883
BV421 anti-human PD-1 antibody (clone EH12.2H7)	BioLegend	Cat#: 329920; RRID: AB_2563884
BV605 anti-human PD-1 antibody (clone EH12.2H7)	BioLegend	Cat#: 329924; RRID: AB_2563885
BV785 anti-human PD-1 antibody (clone EH12.2H7)	BioLegend	Cat#: 329930; RRID: AB_2563886

(*Continued on next page*)

Continued

REAGENT or RESOURCE	SOURCE	IDENTIFIER
PE anti-human PD-1 antibody (clone EH12.2H7)	BioLegend	Cat#: 329906; RRID: AB_2563887
BV421 anti-rabbit IgG antibody (clone Poly4064)	BioLegend	Cat#: 406410; RRID: AB_2563888
PE anti-rabbit IgG antibody (clone Poly4064)	BioLegend	Cat#: 406421; RRID: AB_2563889
PE anti-human CD326 antibody (clone 1B7)	Thermo Fisher Scientific	Cat#: 12-9326-42; RRID: AB_2563890
PE-Cy7 anti-human TNF antibody (clone MP6-XT22)	Thermo Fisher Scientific	Cat#: 25-7321-82; RRID: AB_2563891
PE anti-human Foxp3 antibody (clone PCH101)	Thermo Fisher Scientific	Cat#: 12-4776-42; RRID: AB_2563892
PE-Cy7 anti-human CD39 antibody (clone eBioA1)	Thermo Fisher Scientific	Cat#: 25-0399-42; RRID: AB_2563893
FITC anti-human CCR7 antibody (clone #150503)	R&D Systems	Cat#: FAB197F-100; RRID: AB_2563894
Anti-human/mouse TCF1 antibody (clone C63D9)	Cell Signaling Technology	Cat#: 2203S; RRID: AB_2563895
TotalSeq C0144 anti-human CD183 antibody (clone J252D4)	BioLegend	Cat#: 356939; RRID: AB_2800968
TotalSeq C0140 anti-human CD183 antibody (clone G025H7)	BioLegend	Cat#: 353747; RRID: AB_2800949
TotalSeq C0577 anti-human CD73 antibody (clone AD2)	BioLegend	Cat#: 344031; RRID: AB_2800916
TotalSeq C0386 anti-human CD28 antibody (clone CD28.2)	BioLegend	Cat#: 302963; RRID: AB_2800937
TotalSeq C0141 anti-human CD195 antibody (clone J418F1)	BioLegend	Cat#: 359137; RRID: AB_2810570
TotalSeq C0148 anti-human CD197 antibody (clone G043H7)	BioLegend	Cat#: 353251; RRID: AB_2800943
TotalSeq C0944 anti-human CD101 antibody (clone BB27)	BioLegend	Cat#: 331017; RRID: AB_2832651
TotalSeq C0368 anti-human CD226 antibody (clone 11A8)	BioLegend	Cat#: 338337; RRID: AB_2800933
TotalSeq C0063 anti-human CD45RA antibody (clone HI100)	BioLegend	Cat#: 304163; RRID: AB_2800913
TotalSeq C0179 anti-human CX3CR1 antibody (clone K0124E1)	BioLegend	Cat#: 355705; RRID: AB_2800960
TotalSeq C0089 anti-human TIGIT antibody (clone A15153G)	BioLegend	Cat#: 372729; RRID: AB_2801021
TotalSeq C0146 anti-human CD69 antibody (clone FN50)	BioLegend	Cat#: 310951; RRID: AB_2800810
TotalSeq C0145 anti-human CD103 antibody (clone Ber-ACT8)	BioLegend	Cat#: 350233; RRID: AB_2800967
TotalSeq C0152 anti-human CD223 antibody (clone 11C3C65)	BioLegend	Cat#: 369335; RRID: AB_2814327
TotalSeq C0088 anti-human CD279 antibody (clone EH12.2H7)	BioLegend	Cat#: 329963; RRID: AB_2800862
TotalSeq C0176 anti-human CD39 antibody (clone A1)	BioLegend	Cat#: 328237; RRID: AB_2800965
TotalSeq C0169 anti-human CD366 antibody (clone F38-2E2)	BioLegend	Cat#: 345049; RRID: AB_2800939
TotalSeq C0389 anti-human CD38 antibody (clone HIT2)	BioLegend	Cat#: 303543; RRID: AB_2800938
TotalSeq C0355 anti-human CD137 antibody (clone 4B4-1)	BioLegend	Cat#: 309839; RRID: AB_2800936
Anti-FITC antibody (clone FIT-22)	BioLegend	Cat#: 408302; RRID: AB_528901
Anti-human CD3 antibody (clone OKT3)	Miltenyi Biotec	Cat#: 130-093-387; RRID: AB_1036144
Mouse IgG2a, κ isotype ctrl antibody (clone MOPC-173)	BioLegend	Cat#: 400202; RRID: AB_2927399
Anti-human HLA-A,B,C antibody (clone W6/32)	BioLegend	Cat#: 311402; RRID: AB_314871
GoInVivo Mouse IgG1, κ isotype ctrl antibody (clone MOPC-21)	BioLegend	Cat#: 400190; RRID: AB_3097008
GoInVivo anti-human PD-1 antibody (clone EH12.2H7)	BioLegend	Cat#: 329943; RRID: AB_2565904
Anti-human CD8 antibody (clone SP57)	Roche Diagnostics	Cat#: 790–4460; RRID: AB_2335985
Anti-human/mouse CD39 antibody (clone EPR20627)	abcam	Cat#: ab223842; RRID: AB_2889212
CD8 alpha Monoclonal Antibody (clone C8/144B)	Thermo Fisher Scientific	Cat#: MA5-13473; RRID: AB_11000353
Chemicals, peptides, and recombinant proteins		
Lymphocyte separation medium	Corning	Cat#: 25-072-CV
Dimethyl sulfoxide	Sigma-Aldrich	Cat#: D2650-100ML
LIVE/DEAD Fixable Aqua stain	Thermo Fisher Scientific	Cat#: L34957
LIVE/DEAD Fixable Red stain	Thermo Fisher Scientific	Cat#: L23102
LIVE/DEAD Fixable Near-IR (780) stain	Thermo Fisher Scientific	Cat#: L34993
Dasatinib	Sigma-Aldrich	Cat#: SML2589
FcR blocking reagent, human	Miltenyi Biotec	Cat#: 130-059-901
HLA-A*0201 multimer for CAIX254–262	Immudex	Cat#: WB5683-FITC
Human IL-2 recombinant protein	Peprotech	Cat#: 200-02-50UG
BD GolgiPlug Protein Transport Inhibitor (Containing Brefeldin A)	BD Biosciences	Cat#: 555029

(*Continued on next page*)

Continued

REAGENT or RESOURCE	SOURCE	IDENTIFIER
BD GolgiStop Protein Transport Inhibitor (Containing Monensin)	BD Biosciences	Cat#: 554724
ARL 67156 trisodium salt	Tocris Bioscience	Cat#: 1283
Forskolin	Tocris Bioscience	Cat#: 1099
cAMPS-Rp, triethylammonium salt	Tocris Bioscience	Cat#: 1337
ATP solution	Thermo Fisher Scientific	Cat#: R0441
Critical commercial assays		
Tumor Dissociation Kit, human	Miltenyi Biotec	Cat#: 130-095-929
Foxp3/Transcription Factor Staining Buffer Set	Thermo Fisher Scientific	Cat#: 00-5523-00
Hypoxia Green Reagent for Flow Cytometry	Thermo Fisher Scientific	Cat#: H20035
Chromium Next GEM Single Cell 5′ Library & Gel Bead Kit	10x Genomics	Cat#: PN-1000165
Chromium Single Cell 5′ Library Construction Kit	10x Genomics	Cat#: PN-1000020
Chromium Single Cell 5′ Feature Barcode Library Kit	10x Genomics	Cat#: PN-1000080
Chromium Single Cell V(D)J Enrichment Kit, Human T cell	10x Genomics	Cat#: PN-1000005
Chromium Next GEM Chip G Single Cell Kit	10x Genomics	Cat#: PN-1000120
Single Index Kit T Set A	10x Genomics	Cat#: PN-1000213
Single Index Kit N Set A	10x Genomics	Cat#: PN-1000212
CD8 Microbeads, human	Miltenyi Biotec	Cat#: 130-045-201
CD326 (EpCAM) Microbeads, human	Miltenyi Biotec	Cat#: 130-061-101
Anti-PE Microbeads	Miltenyi Biotec	Cat#: 130-048-801
CellTrace Violet Cell Proliferation Kit	Thermo Fisher Scientific	Cat#: C34557
CellTrace CFSE Cell Proliferation Kit	Thermo Fisher Scientific	Cat#: C34554
SMARTer Human TCR a/b Profiling Kit	Takara Bio	Cat#: 635014
Agilent high sensitivity DNA kit	Agilent	Cat#: 5067-4626
Dynabeads Human T-Activator CD3/CD28 for T cell Expansion and Activation	Thermo Fisher Scientific	Cat#: 11132D
ATP determination kit	Thermo Fisher Scientific	Cat#: A22066
cAMP Parameter Assay	R&D Systems	Cat#: SKGE002B
Deposited data		
Single cell sequencing data	GEO database	GEO: GSE285701
Raw WES data	NCBI Sequencing Read Archive	PRJNA 1200786
Whole transcriptome sequencing data	This paper	Table S9
Software and algorithms		
Cell Ranger 3.1.0	10x Genomics	http://10xgenomics.com
Seurat 4.3.0	Hao et al.	https://satijalab.org/seurat
Harmony 1.2.0	Korsunsky et al.	https://github.com/immunogenomics/harmony
MixCR 3.0.13	Dmitriy et al.	https://github.com/milaboratory/mixcr
R 4.1.0	R Core	https://www.r-project.org
Optitype 1.3.3	Szolek et al.	https://github.com/FRED-2/OptiType
Monocle 2	Cao et al.	https://github.com/MaxMeieran/monocle2
BWA 0.7.17	Li et al.	https://github.com/lh3/bwa
Picard 2.18.2		https://broadinstitute.github.io/picard/
GATK 4.0.5.1	DePristo et al.	https://gatk.broadinstitute.org/hc/en-us
SnpEff 4.3.0	Cingolani et al.	https://github.com/pcingola/SnpEff
dbNSFP 3.5c	Liu et al.	https://www.dbnsfp.org/
Sequenza 3.0.0	Favero et al.	http://www.cbs.dtu.dk/biotools/sequenza/
GISTIC2 2.0.23	Mermel et al.	https://github.com/broadinstitute/gistic2
STAR 2.5.2a	Dobin et al.	https://github.com/alexdobin/STAR

(*Continued on next page*)

Continued

REAGENT or RESOURCE	SOURCE	IDENTIFIER
DESeq2 1.38.3	Love et al.	https://bioconductor.org/packages/release/bioc/html/DESeq2.html
GSVA 1.46.0	Hanzelmann et al.	https://github.com/rcastelo/GSVA
reaConverter 7.0	Reasoft	https://www.reaconverter.com
Adobe Photoshop CS5.5	Adobe	N/A
CellProfiler 4.0.7	McQuin et al.	https://github.com/CellProfiler/CellProfiler
GraphPad Prism 7	GraphPad	N/A
Flowjo 10.8.1	Treestar	https://www.flowjo.com
Other		
gentleMACS Octo Dissociator with Heaters	Miltenyi Biotec	Cat#: 130-134-029
gentleMACS C tubes	Miltenyi Biotec	Cat#: 130-093-237
LSR II instrument	BD Biosciences	N/A
FACSAria II cell sorter	BD Biosciences	N/A
Agilent 2100 bioanalyzer	Agilent	N/A
Bond-Max Fully Automated IHC and ISH Staining System	Leica Biosystems	N/A
Aperio AT2	Leica Biosystems	N/A
M2 Microplate reader	SpectraMax	N/A

EXPERIMENTAL MODEL AND STUDY PARTICIPANT DETAILS

Human specimens

Clinical samples were obtained from patients with RCC ($n = 128$), who underwent surgical resection at Samsung Medical Center. For comparison with RCC, we also obtained tumor samples from patients with breast cancer (Severance Hospital, $n = 131$), hepatocellular carcinoma (Asan Medical Center, $n = 14$), liver cholangiocarcinoma (Asan Medical Center, $n = 10$), ovarian cancer (Severance Hospital, $n = 17$), stomach cancer (Severance Hospital, $n = 32$), head and neck cancer (Ajou University Hospital, $n = 19$), and melanoma (Severance Hospital, $n = 6$), who underwent surgical resection. Tumor tissues samples (0.5–1.0 cm^3) were obtained from patients who underwent surgery with curative intent for their cancer, all of whom provided written informed consent after receiving comprehensive information about the study protocol. This study was approved by the institutional review boards of Samsung Medical Center (IRB Number: 2018-04-037-008), Asan Medical Center (IRB Number: 2016-0845), Ajou University Hospital (IRB Number: AJOUIRB-SMP-2019-355), and Severance Hospital (IRB Numbers: 2013-1071-001, 4-2014-0054, 4-2016-0406, 2018-0173, and 4-2024-1185), and carried out in accordance with the Declaration of Helsinki. The clinical information for patients involved in this study is detailed in Table S2. Patients were retrospectively stratified according to CD39 expression as determined by flow cytometry.

METHOD DETAILS

Single cell collection

Peripheral blood mononuclear cells (PBMCs) were isolated via density gradient centrifugation using lymphocyte separation medium (Corning) from peripheral blood collected at the time of surgery in EDTA anticoagulant tubes. To obtain single-cell suspension of tissues, tumor and normal adjacent tissues were mechanically homogenized using the gentleMACS Octo Dissociator and gentleMACS C tubes (Miltenyi Biotec), enzymatically dissociated into single-cell suspensions using the Tumor Dissociation Kit (Miltenyi Biotec) following the manufacturer's instructions, and then dispersed through a 70-µm filter. Isolated PBMCs and single-cell suspensions were cryopreserved in freezing medium containing 10% dimethyl sulfoxide, and stored in liquid nitrogen at −80°C until use.

Flow cytometry

After single-cell samples were thawed, dead cells were gated out using the LIVE/DEAD fixable dead cell stain kit (Thermo Fisher Scientific). Next, the cells were washed with staining buffer (BD Biosciences), and then stained with fluorochrome-conjugated antibodies against surface proteins for 30 min at 4°C. To stain intracellular proteins, the cells were fixed and permeabilized using the Foxp3 staining buffer kit (Thermo Fisher Scientific), and then stained with fluorochrome-conjugated antibodies. The antibodies used for multicolour flow cytometry are listed in the key resources table. For staining multimers, cells were incubated with dasatinib (50 nM; Sigma-Aldrich) for 15 min at 37°C, and then with FcR blocker (Miltenyi Biotec) for 10 min at 4°C. Next, the cells were stained with fluorochrome-conjugated HLA-A*0201 multimer for $CAIX_{254–262}$ (HLSTAFARV; Immudex) for 15 min at room temperature, and then incubated with anti-FITC antibody (Biolegend) for 15 min at room temperature. Hypoxic status was evaluated using Hypoxia

Green Reagent (Thermo Fisher Scientific), following the manufacturer's instructions. Flow cytometric analyses were conducted using an LSR II instrument (BD Biosciences), and the data were analyzed with FlowJo software (Treestar).

Single-cell library preparation

From single-cell suspensions of tumors and PBMCs, $CCR7^-CD45RA^-$ and $CCR7^-CD45RA^+$ $CD8^+$ T cells were sorted using a FACSAria II cell sorter and stained with antibody-derived tags (ADTs) and hashtags. ADTs and hashtags for CITE-seq are listed in the key resources table. Next, these cells were loaded onto the 10× Genomics Chromium Single Cell platform, and the manufacturer's protocol was followed to perform a comprehensive analysis of the transcriptome, cell-surface protein, and T cell antigen receptor repertoire at the individual single-cell level. Libraries for 5′ transcriptome (RNA), ADT, and T cell receptor (TCR) V(D)J sequences were constructed, following the standard manufacturer's protocol from the 10× Genomics Single Cell Immune Profiling Kit, and were sequenced using Illumina HiSeq systems.

Single-cell sequencing data processing

All single-cell sequencing data were aligned to the GRCh38 reference genome, and processed using the Cell Ranger pipeline. The filtered feature-barcode count matrices and TCR V(D)J annotation files passed quality control in the Cell Ranger pipeline (v3.1.0), and were analyzed using the Seurat R package (v4.3.0).[40] For additional quality control, all subsequent analyses excluded cells with <200 or >2,000 detected genes, and cells with >10% mitochondrial gene expression in RNA UMI counts. We also filtered out cells with detected protein expression of <100 or >10,000 in ADT UMI counts, to avoid antibody aggregation and ensure sufficient cell-surface protein expression data.

Single-cell sequencing clustering and annotation

To prevent clustering driven by the expressions of different TCR genes, we removed TCR-encoding genes from UMI count matrices before further analysis. After filtering and exclusion, gene expression matrices were normalized to the total UMI counts per cell, and transformed to the natural log scale. Next, principal component analysis (PCA) was performed based on 2,000 highly variable feature genes selected using the Seurat package. To eliminate batch effects and ensure the comparability of single-cell data from different patients, we applied the Harmony algorithm (v1.2.0)[41] to each patient's single-cell compartment. The shared nearest neighbor (SNN) modularity optimization-based clustering algorithm was used to identify cell clusters, which were visualized using the uniform manifold approximation and projection (UMAP) dimensional reduction method. Cell types were annotated based on the expressions of previously reported canonical/functional/specific markers[42] and differentially expressed genes (DEGs) between unbiased clusters. Single-cell differential expression analyses were conducted using default parameters, with only positive markers returned. Unsupervised clustering revealed effector memory, terminally-differentiated effector memory, cytotoxic, exhausted, and proliferating $CD8^+$ T cells. These cell types were characterized by their high gene expression levels of *IL7R*, *GZMB/PRF1*, *GZMA/GZMK*, *PDCD1/CTLA4*, and *MKI67/STMN1*, respectively (Figures S1A).

Single-cell surface protein expression analysis

CITE-seq data analysis was performed using the Seurat R package (v4.3.0). The expressions of feature markers were visualized using kernel density estimation (KDE) on UMAP, after centered log-ratio (CLR) normalization of ADT UMI count data. Additionally, we performed *in silico* gating of $CD8^+$ T cells to classify subsets based on PD-1 and CD39 protein expression. Thresholds were determined at the inflection point between the two highest density estimation values for each marker.

Tumor-specificity verification of $CD8^+$ T cells

From single-cell suspensions of tumors, $EPCAM^+$ cells were sorted using CD326 (EPCAM) Microbeads (Miltenyi Biotec), following the manufacturer's instructions, and were cryopreserved. $CD8^+$ TILs were sorted from $EPCAM^-$ cells using CD8 Microbeads (Miltenyi Biotec), and then subjected to flow cytometric sorting using a FACS Aria II cell sorter (BD Biosciences) to obtain $CD39^-CD8^+$ TILs and $CD39^+CD8^+$ TILs. The sorted TILs were expanded using the rapid expansion described in a previous study.[43] Briefly, the $CD39^-CD8^+$ TILs and $CD39^+CD8^+$ TILs were cultured for 2 weeks in 200 μL AIM-V medium (Thermo Fisher Scientific) supplemented with 10% fetal bovine serum (Corning), interleukin-2 (3000 IU mL^{-1}; Peprotech), and 1% penicillin/streptomycin (Sigma), in the presence of anti-CD3 antibodies (30 ng mL^{-1}; Miltenyi Biotec), and irradiated $EPCAM^-CD8^-$ feeder cells. Twice per week, half of the medium was exchanged, and the PD-1 expression level was evaluated. When the number of cells per well exceeded 1×10^6, the cells were transferred to a 48-well plate at a density of 1×10^6/mL. After 2 weeks of culture, expanded $CD8^+$ T cells were used for activation-induced marker assays.

For activation-induced marker assays, cryopreserved $EPCAM^+$ cells were thawed and used as stimulator cells presenting tumor antigens. Before the assay, expanded $CD8^+$ T cells from the culture of $CD39^-CD8^+$ TILs or $CD39^+CD8^+$ TILs were preincubated with isotype IgG2a antibody (50 μg mL^{-1}; Biolegend) or anti-MHC class I antibody (50 μg mL^{-1}; Biolegend) for 30 min at 37°C. The responder cells (1×10^5) were stained with CTV, following the manufacturer's instructions, and co-cultured with effector cells (1×10^5) in a round-bottom 96-well plate. The cells were incubated at 37°C for 12 h, and then evaluated for 4-1BB or IFN-γ expression using flow cytometry. For IFN-γ evaluation, Brefeldin A (1:1,000; BD Biosciences) and Monensin (1:1000; BD Biosciences) were added 1 h after co-culture.

Bulk TCR-sequencing and analysis

After activation-induced marker assays, the 4-1BB$^+$ cells among CD8$^+$ T cells from the culture of CD39$^+$CD8$^+$ TILs were sorted using a FACSAria II cell sorter, and used to construct libraries for bulk TCR-sequencing. The cDNA was synthesized from extracted mRNA, and then amplified using the SMARTer Human TCR a/b Profiling Kit (Takara Bio), following the manufacturer's instructions. The amplified cDNA quality was validated using the Agilent high sensitivity DNA kit, and the Agilent 2100 bioanalyzer. The resulting TCRα/β libraries were pooled and sequenced on an Illumina MiSeq system (paired-end 150 bp). Raw reads of sequence data were aligned and assembled by MiXCR (v3.0.13).[44] Extracted TCRα or TCRβ CDR3 repertoires were analyzed in R version 4.1.0. A distinct CDR3 nucleic-acid sequence of the TCRβ chain was considered a clonotype of CD8$^+$ T cells.

Single-cell TCR repertoire analysis

TCR annotation was conducted using the 10× Cell Ranger V(D)J pipeline (v3.1.0), as described above. The TCR clonotype was considered successfully assembled when it comprised paired TCR alpha and beta chains, with either $\alpha\beta$ or $\alpha\alpha\beta$ configurations. Cells having both the same configuration and CDR3 nucleotide sequences in all chains were considered the same TCR clone. To identify tumor-specific clonotypes in single-cell data, tumor-specific cells were defined as those containing CDR3 amino acid sequences of the TCRβ chain that matched tumor-specific clonotypes identified in the above-described bulk TCR sequencing data. To classify virus-specific clonotypes in the single-cell data, we defined virus-specific cells as those containing CDR3 amino acid sequences of the TCRβ chain specific to human cytomegalovirus (hCMV), Epstein-Barr virus (EBV), and influenza A, with matched HLA genotype in a public VDJ database (VDJdb).[45] To ensure reliability of the analysis, we only extracted clonotypes having frequencies of two or more cells. HLA class I genotyping was predicted from scRNA-seq data of each patient using the Optitype tool (v1.3.3).[46]

Pseudotime analysis

We conducted pseudotime analysis using Monocle 2.[47] After removing proliferating cells expressing genes typically associated with the cell cycle, we further analyzed cells having the clonotypes observed in both blood and tumor samples. Pseudotime ordering was based on the expression of DEGs between tumor-specific cells and other cells (q-value <0.01, total expressed count number >10 genes used). Genes related to cellular stress were removed,[48] and the remaining DEGs were used to infer the trajectory using discriminative dimensionality reduction with trees (DDRTree). We calculated the Pearson's correlation between pseudotime and RNA expression. Among the top 100 genes highly correlated with pseudotime (Table S8), we visualized the expressions of *CREM*, *CXCL13*, *HAVCR2*, *LAG3*, *TNFRSF9*, *CTLA4*, *ENTPD1*, *HLA-DQA1*, and *PDCD1*.

Whole exome sequencing analysis

We performed whole exome sequencing of tumor–normal matched pairs in 31 ccRCC patients. Sequence reads generated from the Illumina platform were aligned to the human reference GRCh38, using BWA (v0.7.17). After marking duplicate reads with Picard (v2.18.2), the resulting alignment files were processed using GATK (v4.0.5.1) for insertions and deletions (INDELs) realignment and base quality recalibration. Mutect2 was applied for variant calling to identify putative somatic mutations, which were then annotated using SnpEff and dbNSFP to predict the functional consequences of single-nucleotide variants (SNVs) and INDELs across the genome. We calculated tumor mutational burden (TMB) as the number of exonic non-synonymous SNVs per megabase, and frameshift INDEL (fsINDEL) burden as the number of frameshift INDELs per sample. We simultaneously estimated putative allele-specific copy number (CN) variations for each sample, using Sequenza (v3.0.0). From Sequenza-estimated copy numbers, we detected significantly amplified (copy gain; GISTIC scores 1 or 2) or deleted (copy loss; GISTIC scores −1 or −2) segments across the genome, using GISTIC2[49] with default parameters. We used the OptiType tool to predict the four-digit HLA class I genotype across all samples. Based on the genotyping of HLA-A, HLA-B, and HLA-C genes, patients were grouped according to their zygosity status. Patients having the same allele in any of the three genes were classified as homozygous, and otherwise classified as heterozygous.

Bulk RNA-sequencing and analysis

Whole transcriptome sequencing reads from 19 ccRCC patients were mapped to the hg19 human reference genome using STAR (v2.5.2a), and quantified with transcripts per million (TPM) values using RSEM. Genes with total read counts of zero across all samples were excluded, and then variance stabilizing transformation (VST) was performed for normalization of the count data using DESeq2 (v1.38.3).[50] To estimate variations of hypoxia-related gene set enrichment through the samples, we perform gene set variation analysis (GSVA) using the GSVA R package (v1.46.0).[51] The following hypoxia-related gene sets were used in this study: (i) hypoxia from the H collection of Hallmark, (ii) response to hypoxia from the C5 collection of Gene Ontology biological processes in the MSigDB database, and (iii) HIF1 transcriptional activity from the NCATS BioPlanet database.

TCGA data analysis

We downloaded TCGA RNA sequencing data from 9,814 patients with 32 cancer types, using R package TCGAbiolinks. Following TPM normalization and log-transformation of individual samples, GSVA analysis was performed with hypoxia gene sets, as described above.

Functional capacity evaluation of CD8$^+$ TILs

From single-cell suspensions of tumor, we sorted PD-1^{bright}CD39$^-$ and PD-1^{bright}CD39$^+$CD8$^+$ TILs using CD8 Microbeads (Miltenyi Biotec) and a FACSAria II cell sorter (BD Biosciences). To evaluate cytokine production, sorted cells (5×10^4 cells/well) were seeded in flat-bottom 96-well plates that had been pre-coated overnight with anti-CD3 antibody (1 μg mL^{-1}; clone OKT3; Miltenyi Biotec). These cells were incubated in AIM-V medium (Thermo Fisher Scientific) containing 1% penicillin/streptomycin (Sigma) at 37°C for 1 h, followed by the addition of Brefeldin A (1:1000; BD Biosciences) and Monensin (1:1000; BD Biosciences). After another 5 h, the cells were harvested and stained with fluorochrome-conjugated antibodies, as described above. For proliferation evaluation, the sorted cells (1×10^5 cells/well) were stained with CTV (Invitrogen), following the manufacturer's instructions, and then seeded in round-bottom 96-well plates along with feeder cells, i.e., irradiated CD8$^-$ TILs (2×10^5 cells/well) that were obtained after sorting CD8$^+$ T cells from TILs. After stimulation, these cells were incubated in AIM-V medium (Thermo Fisher Scientific) containing 1% penicillin/streptomycin (Sigma) in the presence of anti-CD3/CD28-coated Dynabeads (bead-to-cell ratio 1:4; Thermo Fisher Scientific), at 37°C for 120 h. Finally, the CTV dilution was measured by flow cytometry.

In vitro functional restoration assay

Single-cell suspensions of tumor were seeded in round-bottom 96-well plates (2×10^5 cells/well) and incubated at 37°C, in AIM-V medium (Thermo Fisher Scientific) containing 1% penicillin/streptomycin (Sigma) in the presence of anti-CD3 antibody (10 ng mL^{-1}; clone OKT3; Miltenyi Biotec). To evaluate proliferative activity, prior to the incubation, the cells were labeled using CTV (Invitrogen), following the manufacturer's instructions. IgG1 isotype control antibody (10 μg mL^{-1}; Biolegend) or anti-PD-1 antibody (10 μg mL^{-1}; Biolegend) was added. CD39 activity was modulated by addition of the NTPDase inhibitor ARL67156 (250 μM; Tocris). To evaluate cytokine production, Brefeldin A (1:1000; BD Biosciences) and Monensin (1:1000; BD Biosciences) were added at 24 h after stimulation. After another 12 h, cells were harvested and stained with fluorochrome-conjugated antibodies, as described above. To evaluate proliferation, cells were harvested at 96 h after stimulation, and the CTV dilution was measured by flow cytometry. Mitotic index was calculated as the number of mitotic events per seeded T cell.

Immunohistochemical stains and analysis

Immunohistochemical analysis was performed using a tissue microarray (TMA) method. Briefly, representative tumor tissue samples (2-mm diameter) were obtained from individual formalin-fixed and paraffin-embedded (FFPE) tissues (donor blocks), and arranged into new recipient paraffin blocks (TMA blocks), using a trephine apparatus. From each ccRCC case, one core tissue was taken, resulting in the creation of five TMAs. From each TMA block, 4-mm-thick sections were cut, deparaffinized, and dehydrated for immunohistochemical staining. Multiplex IHC was performed in the following order—CD8 IHC stain, scan, destain, CD39 IHC stain, scan, destain, haematoxylin stain, and scan—as adopted from a previous reported protocol.[52] CD8 and CD39 IHC staining was performed using CONFIRM anti-CD8 (SP57) rabbit monoclonal primary antibody (Roche Diagnostics) and anti-CD39 antibody (ab223842; 1:2000 dilution; Abcam) with a Bond-Max system (Leica Biosystems). All IHC slides were scanned at a ×40 magnification using Aperio AT2 (Leica Biosystems). SVS scan files were converted to PNG files using reaConverter v7.0 (reasoft, https://www.reaconverter.com/) with the SVS import level 0 option. Next, the PNG files were reduced to 25% size using Adobe Photoshop CS5.5, and then saved in TIFF format. Before analysis, the CD8 and CD39 IHC files for each case were aligned using Photoshop. CellProfiler (v4.0.7) was used to measure CD8$^+$ and CD8$^+$CD39$^+$ cells.[53]

Multiplex immunofluorescence staining and analysis

mIF staining was performed on 4 μm-thick FFPE tissue sections from human ccRCC samples (Severance hospital, IRB: 4-2024-1185) using the OPAL multiplexing system (Akoya Biosciences). Briefly, slides were deparaffinized, rehydrated through graded ethanol series, and subjected to antigen retrieval using AR9 buffer with microwave heating for 15 min. Endogenous autofluorescence was quenched via two consecutive 45-min LED illuminations. Tissue sections were then blocked with Akoya blocking buffer for 10 min. Primary antibodies against CD8 (1:2000, clone C8/144B, Invitrogen, MA5-13473) and CD39 (1:6000, clone EPR20627, Abcam, ab223842) were sequentially applied in distinct staining cycles, each incubated for 1 h at room temperature, followed by washing in TBST (Tris-buffered saline with 0.05% Tween 20). HRP-conjugated polymer detection was used, and tyramide signal amplification was carried out with Opal 780 (CD8) and Opal 480 (CD39) fluorophores. Epitope retrieval was repeated between cycles using microwave heating in AR9 buffer. After staining, slides were counterstained with DAPI and imaged using the PhenoImager Fusion system at 20× magnification. Spectral unmixing and quantification were performed using inForm software (v3.1, Akoya Biosciences).

Stimulation of naive CD8$^+$ T cells

Naive CD8$^+$ T cells (CCR7$^+$CD45RA$^+$CD8$^+$) were sorted from PBMCs of ccRCC patients, using a FACS Aria II cell sorter (BD Biosciences), and then these cells were stained with CTV, following the manufacturer's instructions. The cells were incubated with anti-CD3/CD28 coated Dynabeads (bead-to-cell ratio 1:4; Thermo Fisher Scientific) in AIM-V (Thermo Fisher Scientific) containing 1% penicillin/streptomycin (Sigma). Intracellular cAMP levels were modulated by the addition of Forskolin (10 μM; Tocris) and/or cAMPS-Rp (1 mM; Tocris). After 96 h of incubation, the cells were harvested and stained with fluorochrome-conjugated antibodies, as described above.

Quantification of ATP and adenosine

From single-cell suspensions of tumor, PD-1^{bright}CD39^- and PD-1^{bright}CD39^+ CD8^+ TILs were sorted using a FACS Aria II cell sorter (BD Biosciences), and CD8^+ T cells were magnetically sorted from PBMCs using CD8 Microbeads (Miltenyi Biotec). The isolated cells were incubated in 37°C AIM-V medium (Thermo Fisher Scientific), in round-bottom 96-well plates (5×10^4 cells per well) in the presence of ATP (100 μM; Thermo Fisher Scientific). ARL67156 (250 μM; Tocris) was added to some wells containing PD-1^{bright}CD39^+CD8^+ TILs. The ATP concentration in the culture medium was measured at 30, 60, and 90 min after incubation using an ATP determination kit (Thermo Fisher Scientific). Luminescence or fluorescence signals were detected using an M2 Microplate reader (SpectraMax).

Quantification of intracellular cAMP

PD-1^{bright}CD39^- and PD-1^{bright}CD39^+ CD8^+ TILs (1×10^5 cells) were sorted, as described above, and washed three times with cold PBS. Then these cells were resuspended in cell lysis buffer, and frozen at <20°C and thawed twice to ensure complete lysis. The lysed cells were centrifuged at 4°C to remove cellular debris. Finally, the cAMP levels in the media were measured by enzyme-linked immunosorbent assay using the cAMP Parameter Assay (R&D Systems) according to the manufacturer's instructions.

In vitro suppression assay

PD-1^{bright}CD39^- and PD-1^{bright}CD39^+ CD8^+ TILs were sorted as described above, and were used as effector cells. CD8^+ T cells were magnetically purified from autologous PBMCs, and were used as responder cells. In some experiments, PD-1^{bright}CD39^- and PD-1^{bright}CD39^+ CD8^+ TILs were used as responder and effector cells, respectively. Responder cells were labeled with CTV, and then equal numbers of effector and responder cells were co-cultured in AIM-V medium (Thermo Fisher Scientific) supplemented with 1% penicillin/streptomycin (Sigma). Anti-CD3/CD28-coated Dynabeads (bead-to-cell ratio 1:2; Thermo Fisher Scientific) were added for stimulation. To some wells, we added ATP (10 μM; Thermo Fisher Scientific) and/or ARL67156 (250 μM; Tocris). At 1 h after stimulation, Brefeldin A (1:1,000; BD Biosciences) and Monensin (1:1000; BD Biosciences) were added. After another 12 h, the cells were harvested and stained with fluorochrome-conjugated antibodies, as described above, to assess the cytokine production by responder cells.

Functional assay in CD39-depleted environment

CD8^+ TILs were sorted from single-cell suspensions of tumor using CD8 Microbeads (Miltenyi Biotec). Next, PD-1^{bright}CD39^- and PD-1^{bright}CD39^+ CD8^+ T cells were purified using flow cytometry, and then labeled using CTV and CFSE staining kits (Thermo Fisher Scientific), respectively. From the remnant CD8^- cells, CD39^+ cells were depleted by sequential staining with PE-conjugated anti-CD39 antibody (BD Biosciences) and anti-PE Microbeads (Miltenyi Biotec), followed by magnetic negative selection. Next, the sorted CD8^+ TILs and CD39^-CD8^- TILs were mixed according to their original proportions, to reconstitute a CD39-depleted environment, in which CD8^+ T cells are the only source of CD39. The reconstituted cells were seeded in round-bottom 96-well plates (3×10^5 cells per well) and stimulated with anti-CD3/CD28-coated Dynabeads (bead-to-cell ratio 1:2; Thermo Fisher Scientific). To evaluate cytokine production, Brefeldin A (1:1,000; BD Biosciences) and Monensin (1:1000; BD Biosciences) were added 1 h after stimulation. After another 12 h, the cells were harvested and stained with fluorochrome-conjugated antibodies, as described above.

QUANTIFICATION AND STATISTICAL ANALYSIS

Categorical data are presented as frequencies with percentages. Continuous data are presented as means with standard deviations. Intergroup differences were analyzed using the unpaired Student's T-test or Mann-Whitney U-test, depending on whether the data satisfied the assumption of a normal distribution. Matched samples were compared using the paired Student's t test or Wilcoxon signed-rank test, depending on whether the data satisfied the assumption of a normal distribution. One-way Repeated Measures ANOVA (RM ANOVA) was used to compare the means of three or more groups, when the same subjects were measured multiple times. Kaplan-Meier survival curves were analyzed with a two-sided log rank test. All tests were two-sided. A p value of <0.05 was considered significant, and confidence intervals (CIs) were calculated at the 95th percentile level. GraphPad Prism version 7 (GraphPad Software) or R (version 4.1.0) were used for statistical analyses, and to present the analyzed data as graphs. In flow cytometry, if there were fewer than 100 events of gated subpopulations, the data were excluded from analyses. No statistical method was used to predetermine sample sizes. Experiments were not randomised, and investigators were not blinded. Experiments did not include replicates, since all participants and their data were unique.